symmetry

MDPI

Article

Symmetric Nature of Stress Distribution in the Elastic-Plastic Range of *Pinus L.* Pine Wood Samples Determined Experimentally and Using the Finite Element Method (FEM)

Łukasz Warguła *, Dominik Wojtkowiak, Mateusz Kukla and Krzysztof Talaśka

Institute of Machine Design, Faculty of Mechanical Engineering, Poznan University of Technology, 60-965 Poznań, Poland; dominik.wojtkowiak@put.poznan.pl (D.W.); mateusz.kukla@put.poznan.pl (M.K.); krzysztof.talaska@put.poznan.pl (K.T.)

* Correspondence: lukasz.wargula@put.poznan.pl; Tel.: +48-(61)-665-20-42

Abstract: This article presents the results of experimental research on the mechanical properties of pine wood (*Pinus L.* Sp. Pl. 1000. 1753). In the course of the research process, stress-strain curves were determined for cases of tensile, compression and shear of standardized shapes samples. The collected data set was used to determine several material constants such as: modulus of elasticity, shear modulus or yield point. The aim of the research was to determine the material properties necessary to develop the model used in the finite element analysis (FEM), which demonstrates the symmetrical nature of the stress distribution in the sample. This model will be used to analyze the process of grinding wood base materials in terms of the peak cutting force estimation and the tool geometry influence determination. The main purpose of the developed model will be to determine the maximum stress value necessary to estimate the destructive force for the tested wood sample. The tests were carried out for timber of around 8.74% and 19.9% moisture content (MC). Significant differences were found between the mechanical properties of wood depending on moisture content and the direction of the applied force depending on the arrangement of wood fibers. Unlike other studies in the literature, this one relates to all three stress states (tensile, compression and shear) in all significant directions (anatomical). To verify the usability of the determined mechanical parameters of wood, all three strength tests (tensile, compression and shear) were mapped in the FEM analysis. The accuracy of the model in determining the maximum destructive force of the material is equal to the average 8% (for tensile testing 14%, compression 2.5%, shear 6.5%), while the average coverage of the FEM characteristic with the results of the strength test in the field of elastic-plastic deformations with the adopted ±15% error overlap on average by about 77%. The analyses were performed in the ABAQUS/Standard 2020 program in the field of elastic-plastic deformations. Research with the use of numerical models after extension with a damage model will enable the design of energy-saving and durable grinding machines.

Keywords: tension; compression; shear; elastic modulus; shear modulus; plasticity limit

Citation: Warguła, Ł.; Wojtkowiak, D.; Kukla, M.; Talaśka, K. Symmetric Nature of Stress Distribution in the Elastic-Plastic Range of *Pinus L.* Pine Wood Samples Determined Experimentally and Using the Finite Element Method (FEM). *Symmetry* **2021**, *13*, 39. https://doi.org/10.3390/sym13010039

Received: 13 November 2020
Accepted: 23 December 2020
Published: 29 December 2020

1. Introduction

Modern science recognizes the growing correlation between the sustainable management of wood resources and human health [1,2]. This contributes to an increase in the number of trees, especially in urban areas [3]. Trees in such places contribute to the improvement of air quality and constitute a natural method of its purification [4,5]. They can also be a bioindicator demonstrating exceeding the limits of pollution [6]. However, green infrastructure areas in cities and trees along roads require pruning and cutting processes. This raises an important issue of reducing exhaust emissions coming from machinery for grinding branches [7,8]. This can be achieved through the use of innovative power units [9], systems improving the machine's adaptation to grinding processes [10,11] or alternative fuels that are less harmful to the environment [12,13]. Regardless of the fuel used and

the fuel supply system, the reduction in engine displacement, and thus the power and torque parameters, leads to a reduction in fuel consumption and reduced exhaust gas emissions [14]. More accurate selection of the power and torque of the power unit for the implemented processing procedures requires knowledge of the system load characteristics [15,16]. Determination of material properties and the development of a simulation model may contribute to a more precise selection of power units and may support the design of more effective cutting mechanisms [17,18].

One fast developing direction of wood research are computer simulations oriented toward the possibility of selected wood properties prediction. The increase in the use of computer analyses allows replacing experiments with non-destructive simulation tests. Modeling with the finite element method (FEM) can be distinguished among such studies. The literature includes analyses regarding e.g., elastic-plastic wooden screw connections [19] or other wooden connections [20], modeling of non-linear multiphase materials [21], modeling of wood-based panels properties [22], wood roasting simulations [23], interaction simulations between wood and microwaves [24], analysis of deformation and tension of upholstered furniture [25,26].

There are articles describing the FEM models along with the mechanical load tests on wood samples, whose aim is to validate the proposed calculation models. Such studies are the current research topic, because in 2019 the three-point bending test results of spruce wood were published, whose model was made in the ABAQUS program, characterized by a Pearson's correlation coefficient at the level of $r = 0.994$ [27]. The study of the coniferous wood model in a similar strength test was also carried out in 2020 [28]. In the same year and software, a model of beech wood compression in three longitudinal, radial, and tangential directions was presented, with the accuracy of covering non-linear functions at the level of $R^2 = 0.72$ [29]. The modeling of beech wood compression in the ABAQUS program was also studied by the team of Prof. Malujda, who analyzed the moisture content and temperature influence on the test samples [30]. The absence of material model of scots pine wood (*Pinus L.* Sp. Pl. 1000. 1753) that can be used in FEM analysis is noticed. Knowledge of the mechanical properties of the tested material is essential to achieve its development.

Tests on the properties of timber are available in the literature; however, very often they relate to selected issues only, for example: the bending strength [31,32] or composite wood [33], determination of modulus of elasticity (MOE) [32], properties during compression [34], tensile [35] and surface properties [36]. It is popular to study timber depending on geographical origin (terrain conditions) due to its mechanical properties [36–38]. Such studies were carried out, among others, for pine wood (*Pinus sylvestris L.*) by Chuchala et al. in 2017 in terms of assessing the cutting force with a band saw [37]. It has been shown that the value of power necessary for the cutting process by a band saw can be twice as large depending on the region of Poland where the wood comes from [37]. Pine tree (*Pinus L.*) as a popular species occurring in Europe and Asia is characterized by many test results, which include, inter alia: the impact of drying methods on moisture content and weight change [38], the effect of heat treatment on impregnation [39,40], impact of the effectiveness of plant protection products [41], it is subject to genetic evaluation [42]. Physical, mechanical, and aerodynamic properties of cones [43], energy properties [44] and mechanical properties [45] of fibers [46] or composites [24,47] are also examined.

Determining the cutting force, which can be the basic data for choosing a power unit, is an important issue for designers and recognized in many scientific publications. Models are available to determine the force during cutting with such machines as: circular saw [48–51], band saw [52], chain saw [53], large crusher [54], milling machine [55–58].

However, there are no models for designers of wood chipping machines; moreover, such machines are characterized by five basic types of cutting mechanisms: cylindrical chipper [10], disk chipper [59], drum chipper [60], hammer chipper [61] and spiral chipper [62]. As indicated by Ihnat et al. in 2020, there is a reduction in the size of timber considered to be waste [63] in the carpentry industry. It follows that machines for grinding branches and

remains of carpentry processes will be characterized by lower power demand, as harder pieces of timber (larger sizes of waste) will be used otherwise.

To design more efficient wood grinding machines, strength tests of pine wood were carried out (*Pinus L.* Sp. Pl. 1000. 1753). The aim of this research work was to determine the numerical model of the destructive force for pine wood for various stress cases based on experimental tests. Results concerning tensile, compression and shear of anisotropic material samples in all significant directions are presented. Inter alia, material constants, such as modulus of elasticity or yield stress were determined based on the research. The published results enabled the development of the FEM model, which at this stage of research maps the elastic-plastic nature of the material in all three strength tests (tensile, compression and shear), in accordance with the research aim. It is oriented at determining the maximum value of force (stress) necessary to destroy the tested material. Models of destruction and its practical applications will be presented in further publications of the authors. The model presented then will be used to determine the maximum cutting force required to the design of economic and ecological grinding machines. Accurate knowledge of the tested material will allow validation of the developed models in the future.

2. Materials and Methods

2.1. Methodology of Strength Tests

Measurements in this study were carried out for pine wood (*Pinus L.* Sp. Pl. 1000, 1753—*Scots pine*) available for commercial sale in Poland. Two types of samples were produced. Type 1 consisted of samples acclimatized for 6 months at 20 °C so that they reached a moisture content (MC) of 8.74% ± 0.1%. Type 2 was samples prepared in the same way to achieve moisture content of 19.9% ± 0.1%. For this purpose, a climatic chamber was used. The moisture content was checked with a Mettler Toledo moisture analyzer during conditioning until the desired value was obtained. The measurement consisted of precise weighing of the sample (±0.001 g) and simultaneous drying (change of MC from measured value to oven-dry). Ten specimens were prepared for each RH (relative humidity) level, loading direction and stress type. The average density of the tested samples was 750 kg m^{-3} ± 5%. The samples were cut mechanically from timber free from defects such as knots, rot, etc. They were made from selected logs in order to obtain representative and reproducible test results with respect to European standards, according to which other scientists are testing [64–66]. Nine samples were tested, and the five most convergent were selected for analysis.

The tests were carried out on the MTS Insight testing machine at temperature of 25 °C and air humidity of 40%, with the use of a 50 kN load cell. The applied strain rate for each of the cases was 0.02 mm/s. The static tensile test was carried out on samples with standardized dimensions in the dog-bone shape (Figure 1a) [67]. For the static compression test, cuboidal samples and dedicated equipment for the testing machine were used. The base on which the test sample was placed consisted of two parts with spherical geometry. The convex and concave parts cooperate in such a way as to enable axial transmission of the compressive force (Figure 1b). The static shear test was also performed using dedicated instrumentation (Figure 1c). Its geometry allowed the stress conditions as close to technical shearing as possible.

Due to its unique internal structure, wood follows an orthotropic pattern along the three axes of its biological directions. These directions are: L—longitudinal or fibrous rings, R—perpendicular to the rings, T—tangent to the rings [68]. Therefore, during tensile and compression test, the samples were subjected to loads in all possible directions in relation to the fibers from the timber they were made. These directions were: longitudinal (L), tangent (T) and radial (R) as shown (with geometric dimensions) in Figures 2 and 3. During the shear tests, the samples were loaded transversely to the fibers in the tangential plane, along the fibers in the tangential plane, transversely to the fibers in the radial plane and along the fibers in the radial plane, as shown in Figure 4. This figure also includes the geometrical dimensions of the used samples. The results of similar studies on the mechanical properties

of walnut (*Juglans regia L.*) and cherry (*Prunus avium L.*) timber can be found in [69], while those concerning yew (*Taxus baccata L.*) and spruce (*Picea abies [L.] Karst.*) in [70].

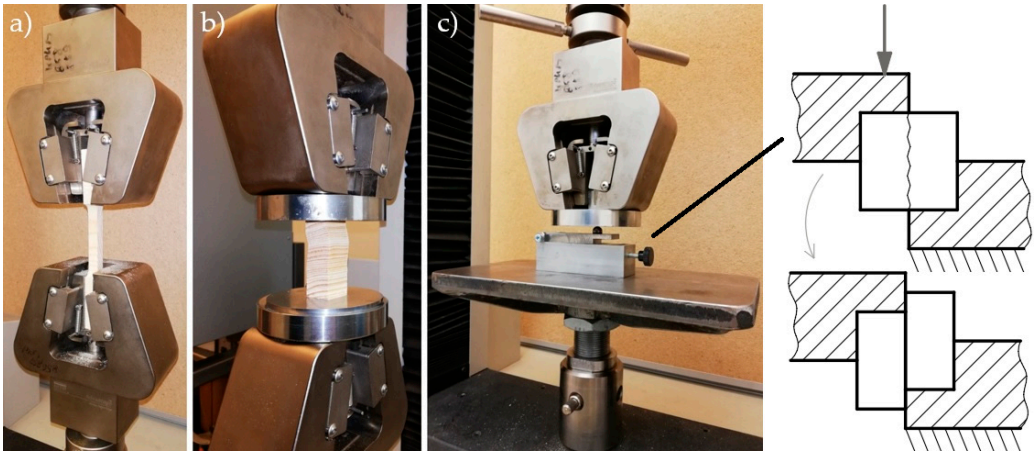

Figure 1. View and diagram of wood testing: (**a**) tensile, (**b**) compression, (**c**) shear.

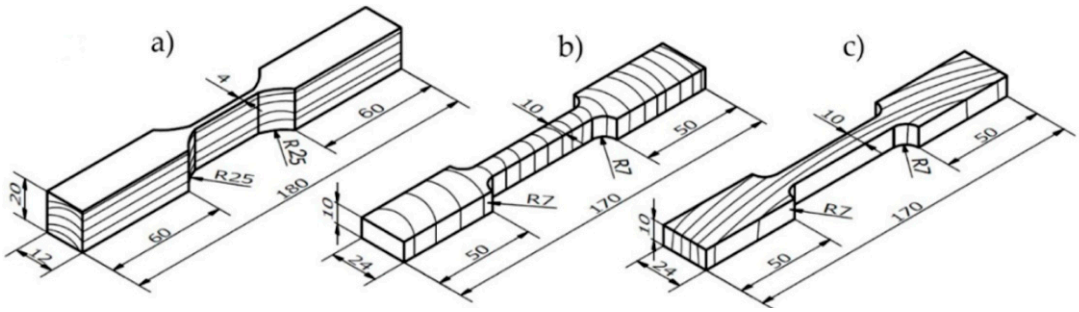

Figure 2. Pine wood samples prepared for tensile testing: (**a**) in the longitudinal direction (L), (**b**) in the radial direction (R), (**c**) in the tangential direction (T).

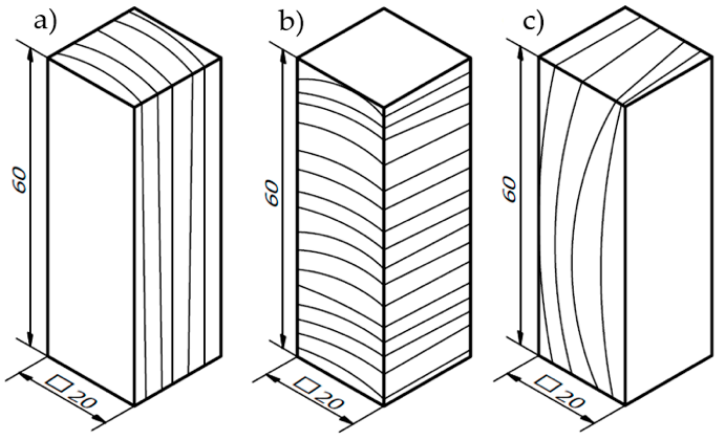

Figure 3. Pine wood samples prepared for compression testing: (**a**) in the longitudinal direction (L), (**b**) in the radial direction (R), (**c**) in the tangential direction (T).

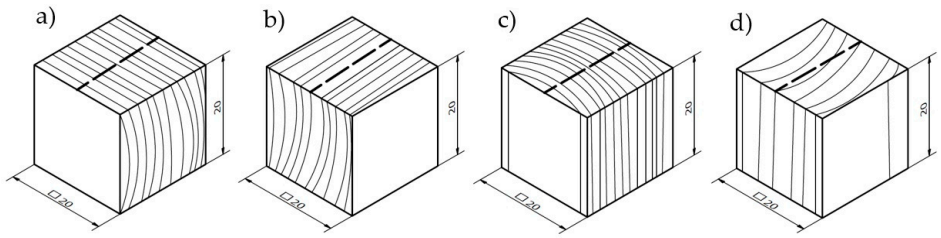

Figure 4. Pine wood samples prepared for shear tests: (**a**) crosswise to the fibers in the tangential plane (TR), (**b**) crosswise to the fibers in the radial plane (RT), (**c**) along the fibers in the radial plane (LR), (**d**) along the fibers in the tangential plane (LT).

The research work consisted of determining the yield point as a result of plotting a straight line tangent to the registered stress-strain curve. This line is defined by two points: the first is the origin of the coordinate system, the second is the point where the curve deviates from the tangent by more than 1% (as schematically shown in Figure 5). The modulus of elasticity was determined based on the inclination angle of the straight line determined in this way. The values for the shear stress tests were determined analogously.

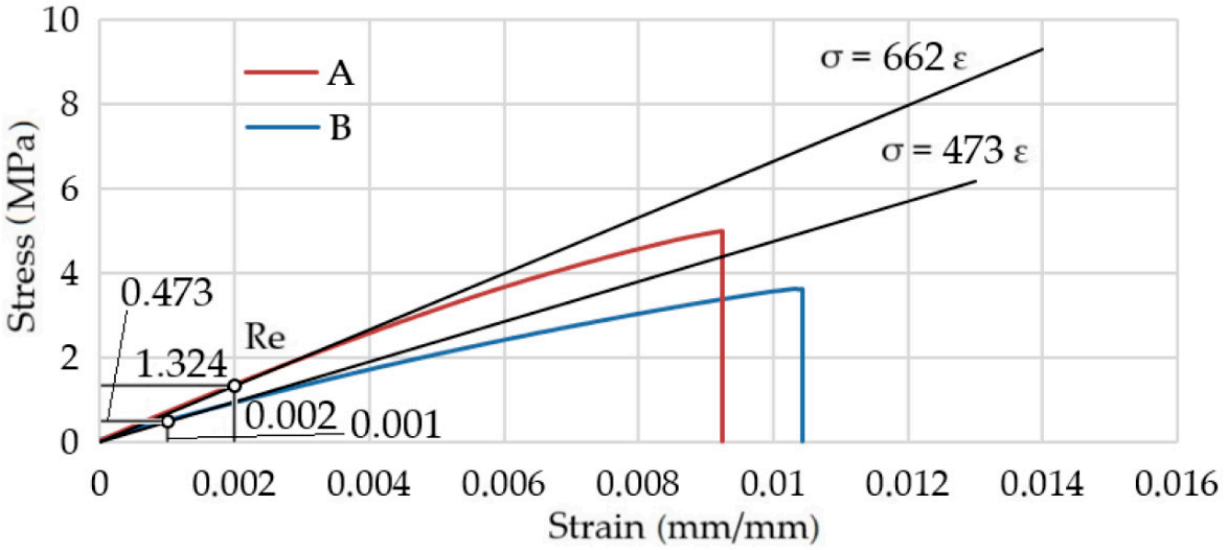

Figure 5. Averaged tensile characteristics and method of determining modulus of elasticity for tested materials during static tensile test; A—sample with 8.74% moisture content, B—sample with 19.9% moisture content.

2.2. Model Finite Element Method (FEM)

The analyses were performed in the ABAQUS/Standard 2020 software. For tensile tests (Figure 6) a 3D model of a paddle sample was made, whose side surfaces (which are in fact compressed by the jaws of the gripper used in the tensile test) of the lower gripping part of the sample were fixed, and the upper ones were given kinematic extortion with a specified displacement value. The sample was divided into finite elements of the type C3D8R: an 8-node linear brick with reduced integration and hourglass control. The results were presented in the form of stress distribution in the stretched sample.

The wood material was modeled as elastic-plastic without considering the failure mechanisms. The elastic part was modeled with the engineering constants that consisted of 3 elastic moduli E_1, E_2 and E_3, 3 Poisson ratios ν_1, ν_2 and ν_3 and 3 shear moduli G_1, G_2 and G_3. The elastic moduli as well as the theoretical Yield Point (which divides the characteristic into elastic and plastic range) were determined based on the experimental test characteristics. If the stress level exceeds the Yield Point value, the behavior of the material was determined based on the tabular relation between the stress and the strain,

which was determined for each of the 18 combinations of three states of stress (tension, compression and shearing), two values of moisture content (samples type 1 and 2) and three directions of wood structure (longitudinal, radial and tangential) separately. The range of the analysis was limited up to the point of the critical strain, where the failure of the material takes place (as was tested in the experimental research).

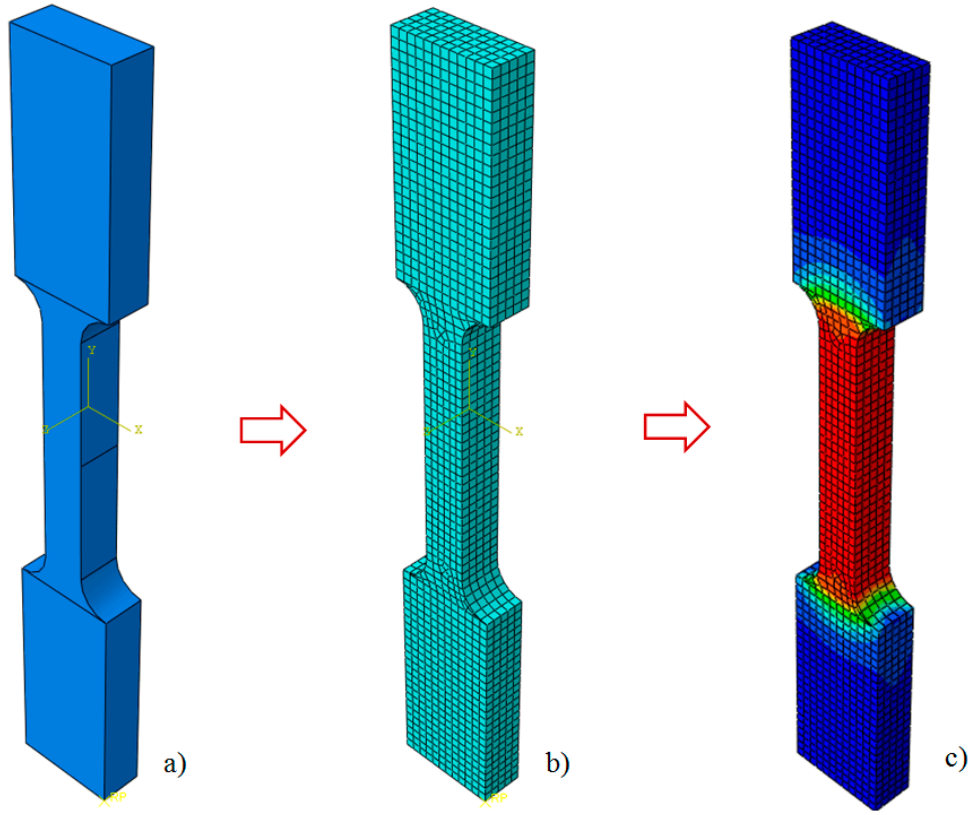

Figure 6. Tensile—model structure: (**a**) solid model, (**b**) meshed model (C3D8R elements), (**c**) results—stress state.

Compression test (Figure 7) was made with the use of a 3D model, which consisted of a tested sample and two jaws—the lower fixed and the upper, to which kinematic extortion with a given displacement value was applied. The C3D8R finite elements were also used in this study, similar to the tensile test. The sample was modeled as a deformable element, while the jaws were modeled as Rigid Bodies. To prevent the sample from escaping due to the lateral force generated on the sample's contact surface with the jaws, sockets blocking the sample movement without generating artificial stress in the sample compression section were made in the jaws. The results were presented in the form of stress distribution in the compressed sample.

To decrease the computational time 2D analysis was used for performing the simulation of the shear test (Figure 8), where the cut section constituted a square with a side of 20 mm. The element was meshed using the CPS4R elements—a 4-node bilinear plane stress quadrilateral with reduced integration and hourglass control. The jaws of the testing device used in the shear test were modeled as straight lines lying on the vertical sides of the cut section. The boundary conditions were applied in such a way that one of the reference points marked in Figure 8c was established, and kinematic extortion with a given displacement value was applied to the other one (located in the opposite corner). The results are presented in the form of stress distribution in the cutting section.

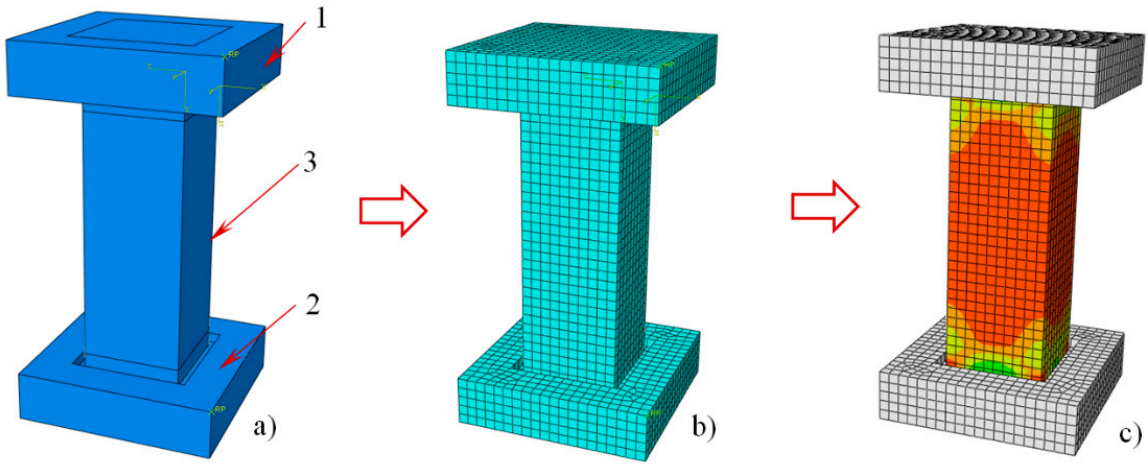

Figure 7. Compression-model structure: (**a**) solid model: 1—upper jaw, 2—lower jaw, 3—sample, (**b**) meshed model (C3D8R elements), (**c**) results—stress state.

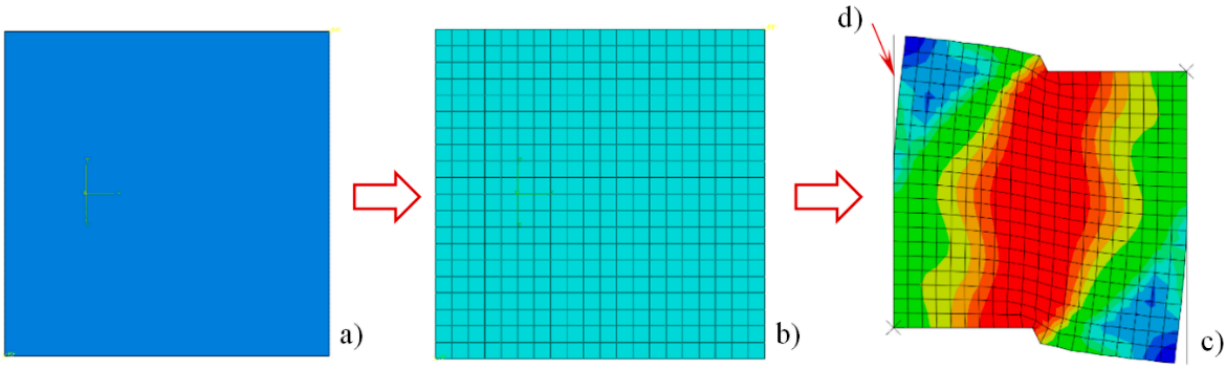

Figure 8. Cutting model construction: (**a**) flat model, (**b**) digitized model (CPS4R elements), (**c**) results—stress state, (**d**) model of the jaw of the device.

In all three studies, contact with a property in the tangential direction defined by a constant value of the friction coefficient of μ = 0.25 [71,72] was used to model the contact between the test sample made of pine wood and the instrumentation made of steel. In the crosswise direction, a "hard contact" property that prevents two elements from interpenetration was defined.

Since 18 different cases were analyzed, it is possible to determine which of these cases provide the greatest challenge for the working unit of the machine. Each case will be valid for a different wood processing technology such as chopping, shredding, cutting, etc. The presented database of models (engineering constants) for the selected types of wood can be used to compare various tools used for wood processing in a chosen technology and to determine the influence of the tool geometry. This approach will be used to improve the design process of the wood processing devices. Since all of these models were obtained based on the same experimental research and using the same methodology, it is safe to state that it will be suitable for the selected purpose. Additionally, the practice of using various simplifications in wood modeling, depending on the application of the model, can be found in the literature [73–76].

3. Results

Material Strength Test Results

Results of the test are the characteristics of static tensile, compression and shear stress-strain curves. Examples of static longitudinal tensile test results are shown in Figure 9. On

their basis, the average tensile characteristics in the longitudinal direction were determined along with the determined modulus of elasticity (Figure 10). The values determined on the basis of a static tensile test in the longitudinal direction (L), radial direction (R), tangential direction (T), for samples with 8.74% and 19.9% moisture content are presented in Table 1.

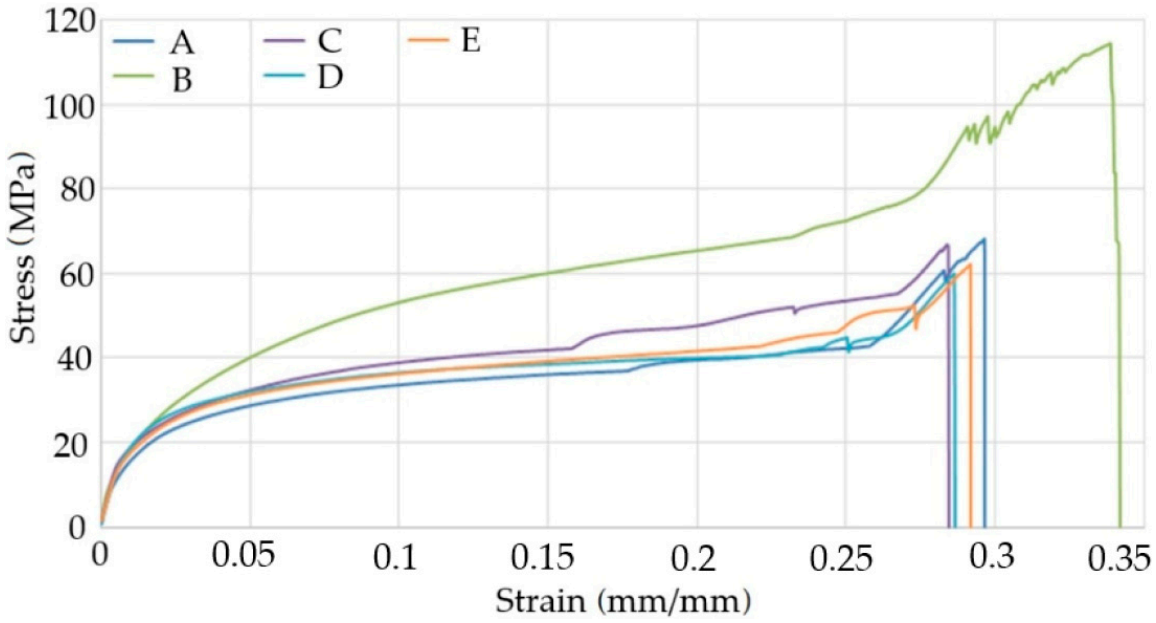

Figure 9. Selected results of the static longitudinal tensile test (moisture content 19.9%); A—sample number 1, B—sample number 2, C—sample number 3, D—sample number 4, E—sample number 5.

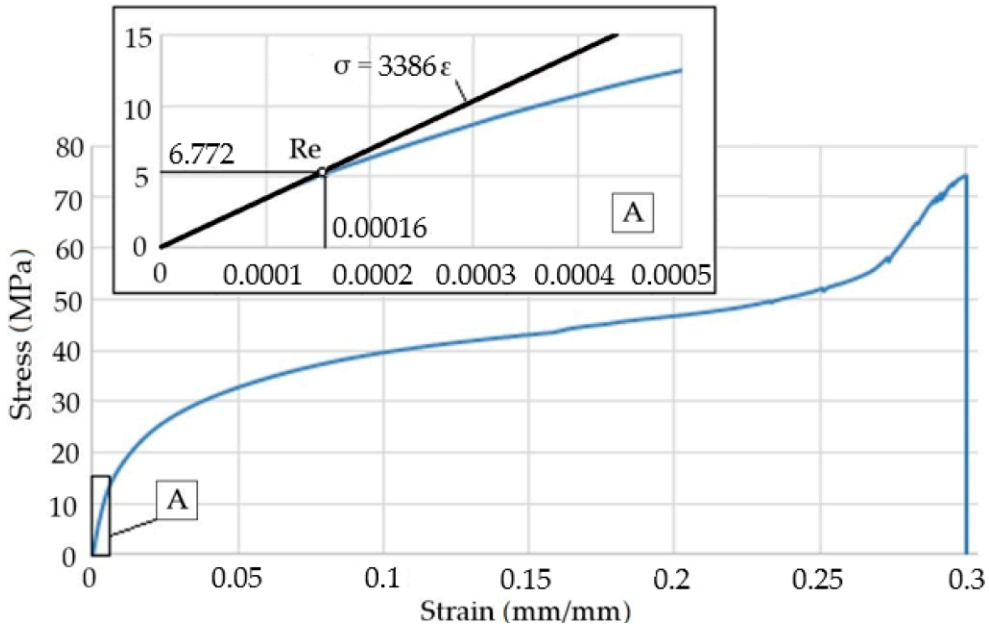

Figure 10. Averaged tensile characteristics and modulus of elasticity determination method for tested materials during static longitudinal tensile test (moisture content 19.9%); A—enlargement of the initial part of the chart.

Table 1. Average values determined on the basis of a static tensile test; L—longitudinal direction, R—radial direction, T—tangential direction.

Direction (Tensile)	**L**		**R**		**T**	
Sample Type	**1**	**2**	**1**	**2**	**1**	**2**
Moisture content [%]	8.74	19.90	8.74	19.90	8.74	19.90
Cross-section area A [mm^2]	80	80	100	100	100	100
Yield point R_e [MPa]	7.675	6.772	1.324	0.473	0.84	0.32
Standard deviation	0.25	0.21	0.09	0.03	0.02	0.02
Deformation ε_e [%]	0.0022	0.0018	0.0028	0.0018	0.0048	0.0030
Standard deviation	0.0002	0.0002	0.0002	0.0002	0.0002	0.0002
Tensile strength R_m [MPa]	76.39	74.28	4.98	3.63	3.28	1.68
Standard deviation	18.64	19.32	0.55	0.25	0.43	0.22
Deformation ε_m [%]	0.16	0.27	0.009	0.011	0.018	0.015
Standard deviation	0.03	0.04	0.0004	0.0005	0.0018	0.0007
Modulus of elasticity E [MPa]	3838	3386	662	473	212	161
Standard deviation	5.66	4.52	2.34	2.55	2.71	3.12

Examples of static radial compression test results are shown in Figure 11. On their basis, the average radial compression characteristics were determined along with the determined moduli of elasticity (Figure 12). The non-linearity visible in the initial measuring range results from the unevenness of the pressed surface of the sample, which only after alignment allows achieving a linear range. The values determined on the basis of a static tensile test in the longitudinal direction (L), radial direction (R), tangential direction (T), for samples with 8.74% and 19.9% moisture content are presented in Table 2.

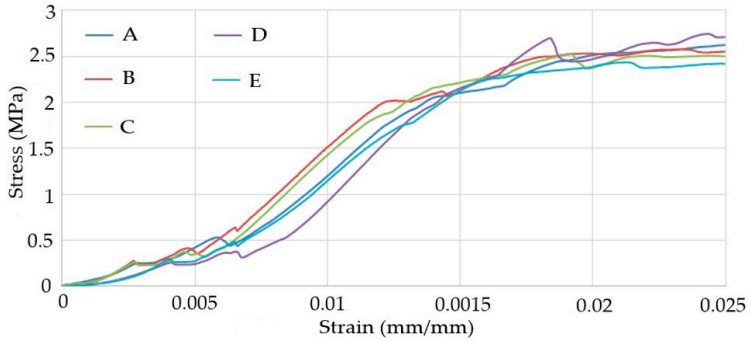

Figure 11. Selected results of the static longitudinal compression test (moisture content 19.9%); A—sample number 1, B—sample number 2, C—sample number 3, D—sample number 4, E—sample number 5.

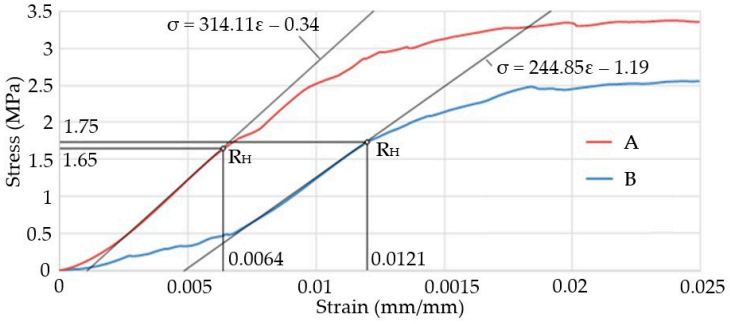

Figure 12. Averaged compression characteristics and method of determining modulus of elasticity for tested materials during static tensile testing; A—sample with 8.74% moisture content, B—sample with 19.9% moisture content.

Table 2. Average values determined on the basis of a static compression test; L—longitudinal direction, R—radial direction, T—tangential direction.

Direction (Compression)	L		R		T	
Sample Type	**1**	**2**	**1**	**2**	**1**	**2**
Moisture content [%]	8.74	19.90	8.74	19.90	8.74	19.90
Cross-section area A [mm^2]	400	400	400	400	400	400
The limit of proportionality R_H [MPa]	43.29	38.16	1.65	1.75	2.09	1.77
Standard deviation	5.1	2.8	0.24	0.33	0.19	0.15
Deformation ε_H [%]	1.86	1.63	0.64	1.21	1.72	1.78
Standard deviation	5.1	2.8	0.24	0.33	0.19	0.15
Modulus of elasticity E [MPa]	3218	3495	314	245	162	145
Standard deviation	5.1	2.8	0.24	0.33	0.19	0.15

Examples of static shear test results along the fibers in the radial plane are shown in Figure 13. On their basis, the average shear characteristics crosswise to the fibers in the radial plane (RT) were determined along with the determined shear moduli (Figure 14). Values determined on the basis of a static compression test crosswise to the fibers in the tangential plane (TR), crosswise to the fibers in the radial plane (RT), along the fibers in the radial plane (LR), along the fibers in the tangential plane (LT), for samples with a moisture content of 8.74% and 19.9% are presented in Table 3.

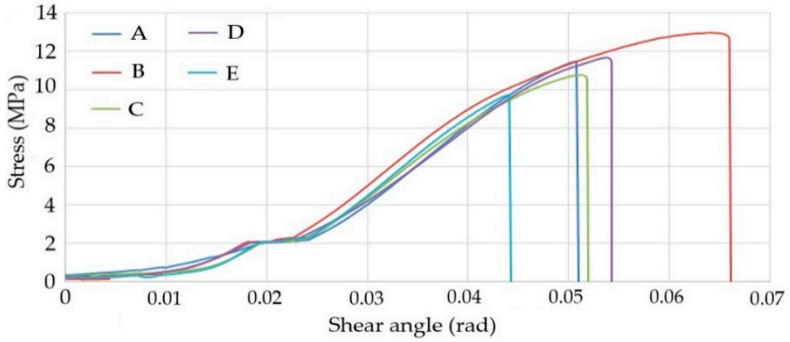

Figure 13. Selected results of the static shear test crosswise to the fibers in the radial plane (RT) (moisture content 19.9%); A—sample number 1, B—sample number 2, C—sample number 3, D—sample number 4, E—sample number 5.

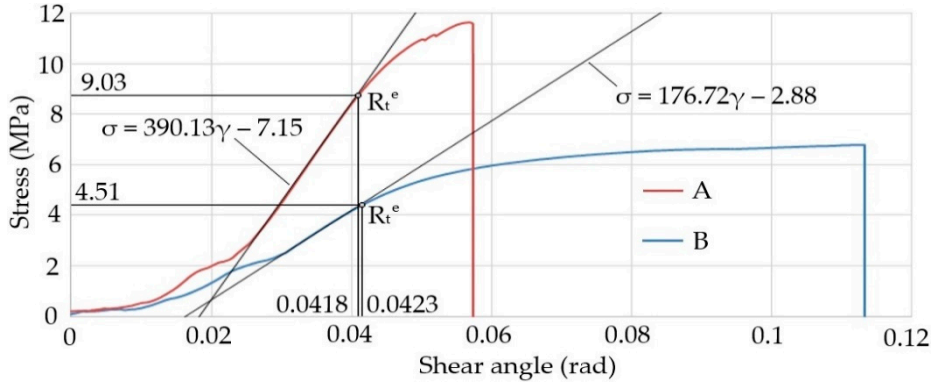

Figure 14. Averaged shear characteristics and method of determining the shear modulus for the tested materials during a static shear test crosswise to the fibers in the radial plane (RT); A—sample with 8.74% moisture content, B—sample with 19.9% moisture content.

Table 3. Average values determined on the basis of a static shear test of a pine sample; crosswise to the fibers in the tangential plane (TR), crosswise to the fibers in the radial plane (RT), along the fibers in the radial plane (LR), along the fibers in the tangential plane (LT).

Direction (Shear)	**TR**		**RT**		**LR**		**LT**	
Sample Type	**1**	**2**	**1**	**2**	**1**	**2**	**1**	**2**
Moisture content [%]	8.74	19.90	8.74	19.90	8.74	19.90	8.74	19.90
Cross section area A [mm^2]	400	400	400	400	400	400	400	400
Yield point for shearing test R_t^e [MPa]	4.74	0.972	1.60	0.61	8.46	1.93	9.03	4.51
Standard deviation	0.14	0.21	0.23	0.28	0.12	0.11	0.21	0.24
Deformation γ_e [%]	9.95	1.74	2.49	4.88	3.88	1.88	4.18	4.23
Standard deviation	0.19	0.20	0.22	0.43	0.16	0.33	0.22	0.23
Shear strength R_t	8.07	3.53	4.15	1.28	14.93	7.01	11.65	6.77
Standard deviation	0.54	0.61	1.04	0.34	1.09	0.71	1.32	0.92
Deformation γ_t [%]	18.30	12.76	12.33	17.78	9.51	10.43	5.74	11.32
Standard deviation	1.73	2.81	2.45	3.03	2.52	0.74	0.75	2.98
Shear modulus G [MPa]	135	99	114	19	372	210	390	177
Standard deviation	2.14	3.21	4.67	8.9	5.13	4.48	2.12	5.61

4. Engineering Constants Used in FEM Modeling of the Wood Test

FEM models require the introduction of material constants, which were determined in the course of research and taken from literature [77]. Moduli of elasticity used to model all three types of tests were determined on the basis of experimental results, similarly to shear moduli used for modeling compression and shear tests. However, the tests did not allow for accurate determination of Poisson's ratio nor for shear moduli for the tensile test. The tables contained in the works of Kretschmann, 2010 [72] were used for this purpose. In the tables the elastic ratios representing the remaining five moduli of elasticity relative to Young's moduli in longitudinal direction were presented for various species. The missing values, which were not specified based on the experimental research, were determined on the basis of the ratio of two extreme moduli of elasticity (in longitudinal and tangential directions) comparing the obtained result in the literature [77]. For that purpose the proper ratios (ET/EL, ER/EL, GLR/EL, GLT/EL, GRT/EL) and based on that closest out of the nine species of Pine was selected (based on Table 5-1 [10]) and then the Poisson ratio were selected (based on Table 5-2 [10]). Since data were presented for only one moisture content (12%) which lie between both values analyzed (8.74% and 19.9%) authors have assumed that since the moisture content affects the mechanical properties, for both dry and wet the specimen will behave as different species of pine wood. The values of the engineering constants for the FEM model used in the tensile test are shown in Table 4, compression in Table 5, and shear in Table 6.

Table 4. Engineering constants used in FEM modeling of the wood tensile test.

Mechanical Parameters	**Moduli of Elasticity**			**Poisson's Ratios**			**Shear Moduli**		
Engineering Constants	**E_1 [MPa]**	**E_2 [MPa]**	**E_3 [MPa]**	**ν_{12} [-]**	**ν_{13} [-]**	**ν_{23} [-]**	**G_{12} [MPa]**	**G_{13} [MPa]**	**G_{23} [MPa]**
Extension 8.74% (MC)	3838	662	212	0.332	0.365	0.384	272.5	230.3	46.1
Extension 19.9% (MC)	3386	473	161	0.392	0.444	0.447	186.2	179.5	33.9

Table 5. Engineering constants used in FEM modeling of the wood compression test.

Mechanical Parameters	**Moduli of Elasticity**			**Poisson's Ratios**			**Shear Moduli**		
Engineering Constants	**E_1 [MPa]**	**E_2 [MPa]**	**E_3 [MPa]**	**ν_{12} [-]**	**ν_{13} [-]**	**ν_{23} [-]**	**G_{12} [MPa]**	**G_{13} [MPa]**	**G_{23} [MPa]**
Compression 8.74% (MC)	3218	314	162	0.332	0.365	0.384	372	390	114
Compression 19.9% (MC)	3495	245	145	0.28	0.364	0.389	210	177	19

Table 6. Engineering constants used in FEM modeling of the wood shear test.

Mechanical Parameters	Moduli of Elasticity			Poisson's Ratios			Shear Moduli		
Engineering Constants	**E_1 [MPa]**	**E_2 [MPa]**	**E_3 [MPa]**	**ν_{12} [-]**	**ν_{13} [-]**	**ν_{23} [-]**	**G_{12} [MPa]**	**G_{13} [MPa]**	**G_{23} [MPa]**
Shear B 8.74% (MC)	314	162	-	0.384	-	-	114	372	390
Shear B 19.9% (MC)	245	145	-	0.389	-	-	19	210	177
Shear C 8.74% (MC)	3218	314	-	0.332	-	-	372	390	114
Shear C 19.9% (MC)	3495	245	-	0.28	-	-	210	177	19
Shear D 8.74% (MC)	3218	162	-	0.365	-	-	390	372	114
Shear D 19.9% (MC)	3495	145	-	0.364	-	-	177	210	19

In this research, 18 FEM analyses were performed as a combination of various parameters. Each of these cases will be valid for different wood processing technologies such as chopping, shredding, cutting, etc. It is not possible to describe all these processes by using a single material model. The main goal is to determine the database of models (engineering constants) for the selected type of wood, which can be used to compare various tools used for wood in a chosen technological process and to find the influence of the tool geometry. This will enable finding effective solutions in terms of tool design for wood machining. Since all of these models were obtained based on the same experimental research and using the same methodology, it is safe to state that they will be usable for the selected purpose.

5. Discussion

5.1. Analysis of the Results of Strength Tests of Tested Samples

Mechanical properties of pine wood (*Pinus L.* Sp. Pl. 1000. 1753) vary depending on the direction of the wood fibers and moisture content. Tensile tests showed a decrease in mechanical properties along with an increase in material moisture (around 11%) in the range from 3% to 64% depending on the parameter, as shown in Figure 15. Wood during the tensile test shows the greatest strength in the longitudinal direction L, then in the radial direction R, and it is the least resistant to tensile forces in the tangential direction T. The nature of the determined properties is consistent with the tests of wood of other scientists [78–81].

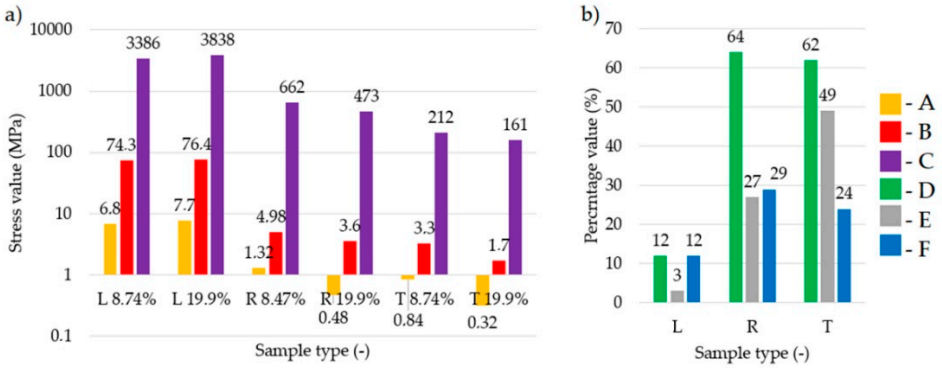

Figure 15. Comparison of mechanical properties due to material moisture content and wood grain direction during tensile test (L—longitudinal direction, R—radial direction, T—tangential direction), (**a**) stress values, (**b**) percentage value, where: A—Yield point, B—Tensile strength, C—Modulus of elasticity, D—Decrease in the yield point of the material due to sample moisture, E—Decrease in the tensile properties of the material due to sample moisture, F—Decrease in the modulus of elasticity value due to sample moisture.

Compression testing showed a change in mechanical properties as the material moisture increased (around 11%), but did not contribute to deterioration in all cases (as opposed to tensile or shear strength tests). Changes in material properties depending on mois-

ture content in the conducted tests ranged from 6% to 22% (Figure 16). Wood during the compression test shows the greatest strength in the longitudinal direction L, then in the tangential direction T, and it is the least resistant to compression forces in the radial direction R. The nature of the determined properties is consistent with the tests of wood of other scientists [78,82].

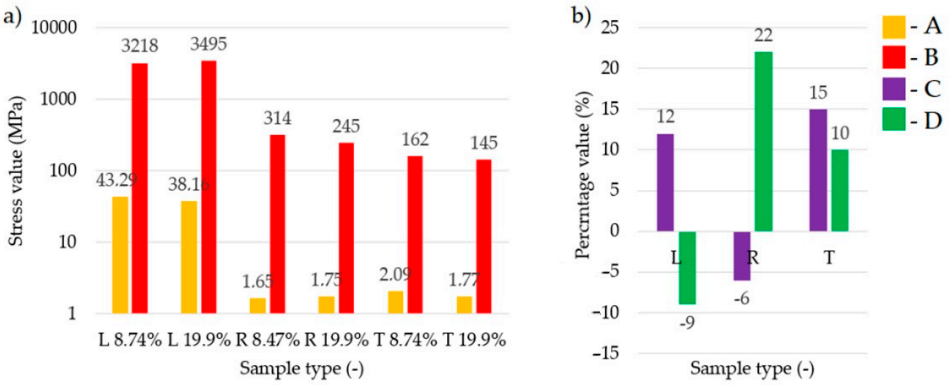

Figure 16. Comparison of mechanical properties due to material moisture content and wood grain direction during compression test (L—longitudinal direction, R—radial direction, T—tangential direction), (**a**) stress values, (**b**) percentage value, where: A—Yield point, B—Modulus of elasticity, C—Change of yield point material due to sample moisture, D—Change of modulus of elasticity modulus value due to sample moisture content.

Shear tests showed a decrease in mechanical properties along with an increase in material moisture content (approximately 11%) in the range of 27% to 83% depending on the parameter, as shown in Figure 17. During the shear test, wood shows the greatest strength along the fibers in the radial plane (LR) and along the fibers in the tangential plane (LT), then in the direction crosswise to the fibers in the tangential plane (TR), and it is the least resistant to shear forces in the crosswise direction for fibers in the radial plane (RT). The nature of the determined properties is consistent with the research of other scientists in relation to wood [77,82].

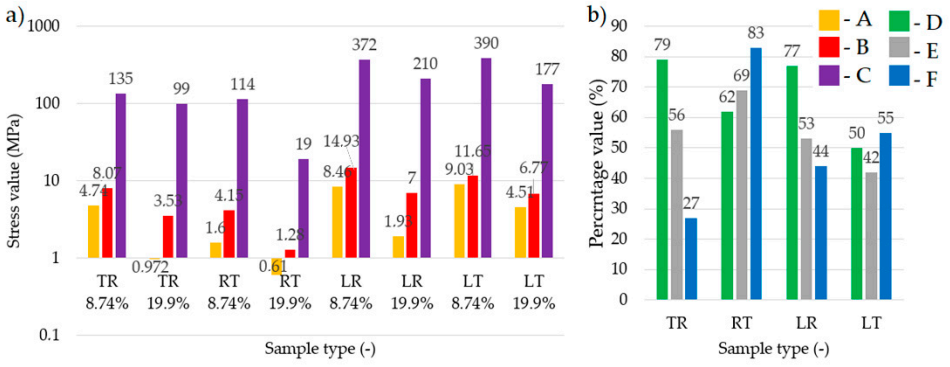

Figure 17. Comparison of mechanical properties due to material moisture content and wood grain direction during shear test (crosswise to fibers in the tangential plane (TR), crosswise to fibers in the radial plane (RT), along the fibers in the radial plane (LR), along the fibers in the tangential plane (LT)), (**a**) stress values, (**b**) percentage value, where: A—Yield point, B—Wall strength, C—Shear modulus, D—Change in material yield point value due to sample moisture, E—Change in mechanical properties on the material wall due to sample moisture, F—Change of shear modulus value due to sample moisture.

5.2. Analysis of FEM Model Results and Strength Test Results

The results of the FEM model showing the material exposed to various strength tests, for both dry and wet specimens (8.74% and 19.9% moisture content), are presented in Figures 18–35. The material characteristics in the elastic-plastic range were presented in relation to the result of tests carried out on the testing machine. The stress state distributions from the FEM model were marked on them in selected fragments of the characteristic (in the case of compression and shear tests at points corresponding to 10%, 50%, and 100% deformation causing sample destruction, while during tensile—the state just before breaking only), which show the stress distribution in tested sample. Due to the purpose of the developed model (determination of the maximum destructive force), it is more important for authors to determine the value of the point corresponding to the material strength limit rather than mapping the characteristics. To evaluate the model, the authors conducted an analysis of the model results discrepancy and strength values in two configurations. The first concerned the maximum destructive force and is presented in Tables 7–9. The second one concerned the mapping of the characteristics and was presented in Tables 10–12, where the coverage of the curve from the test results and the FEM model in the range of ±15% error were analyzed. An example of the analysis of the coverage of the characteristics is shown in Figure 36, the coverage of the characteristic is expressed in accordance with relationship (1):

$$\textit{Characteristic coverage } (\pm 15) = \frac{X - Y}{X} \cdot 100\%, \quad (1)$$

where: X—the length of the characteristics from the strength test, Y—the sum of the lengths of the sections of the FEM model characteristics (±15%) overlapping with the characteristics of the strength tests.

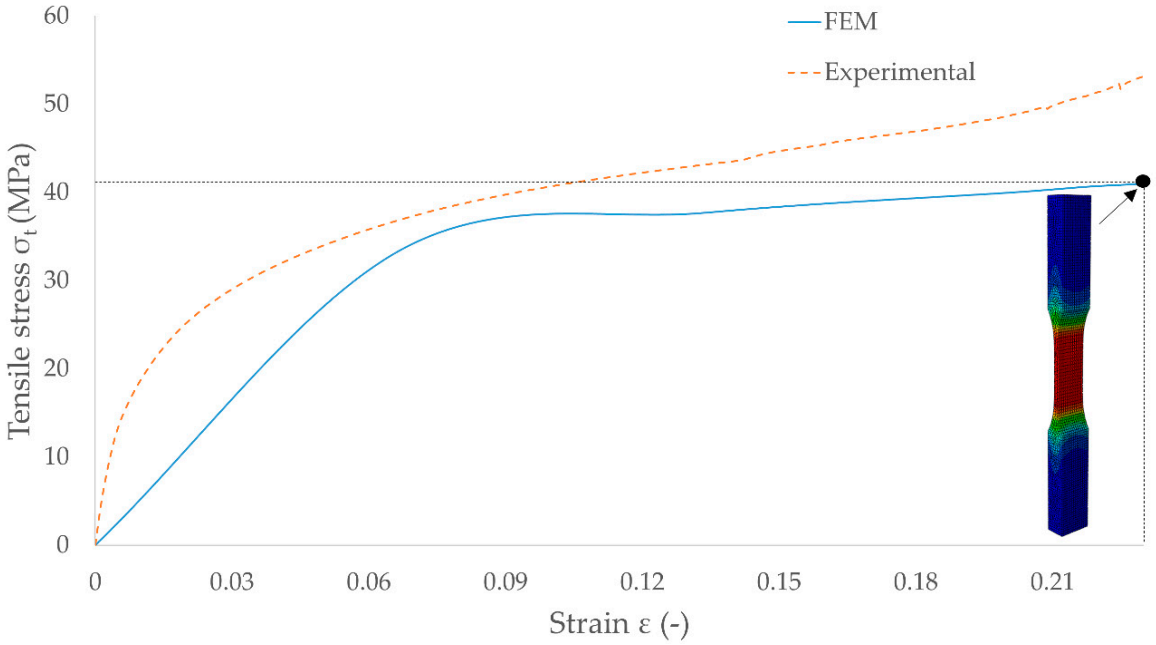

Figure 18. Characteristics of pine wood (*Pinus L.* Sp. Pl. 1000. 1753) with 19.9% moisture content in the longitudinal direction (L) during tensile test obtained from the FEM analysis and compared with the averaged experimental result.

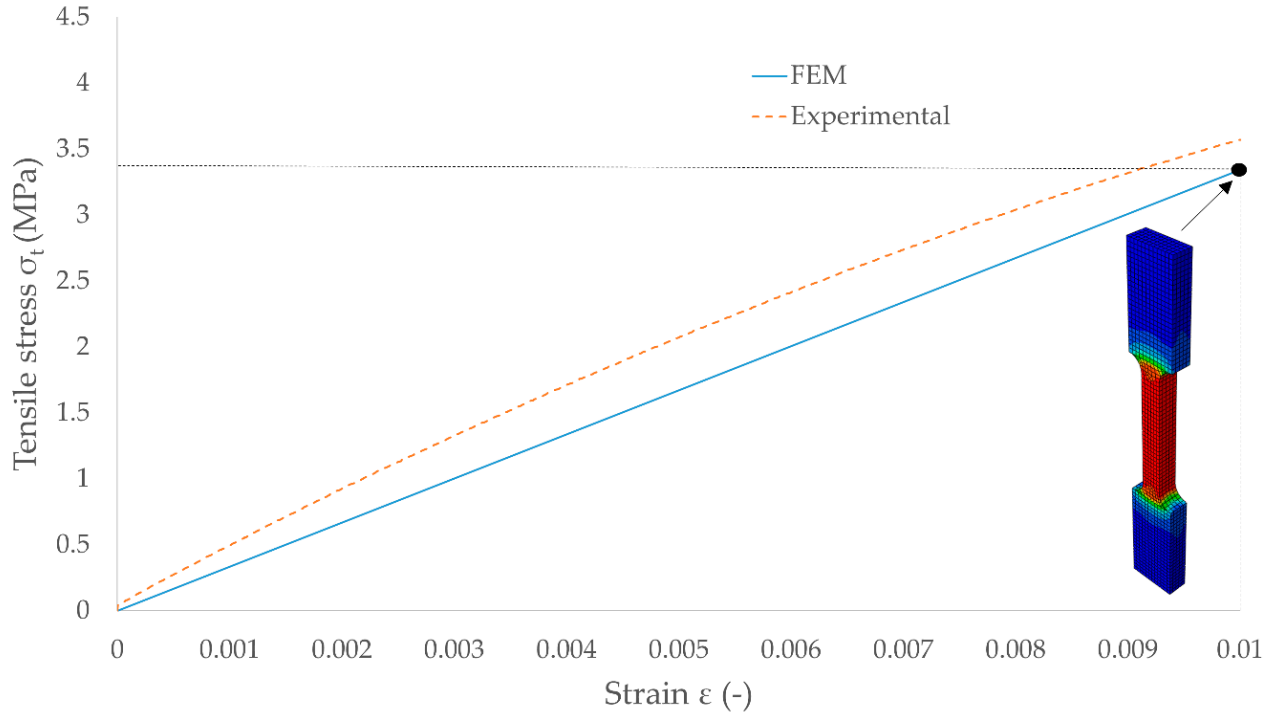

Figure 19. Characteristics of pine wood (*Pinus L.* Sp. Pl. 1000. 1753) with 19.9% moisture content in the radial direction (R) during tensile test obtained from the FEM analysis and compared with the averaged experimental result.

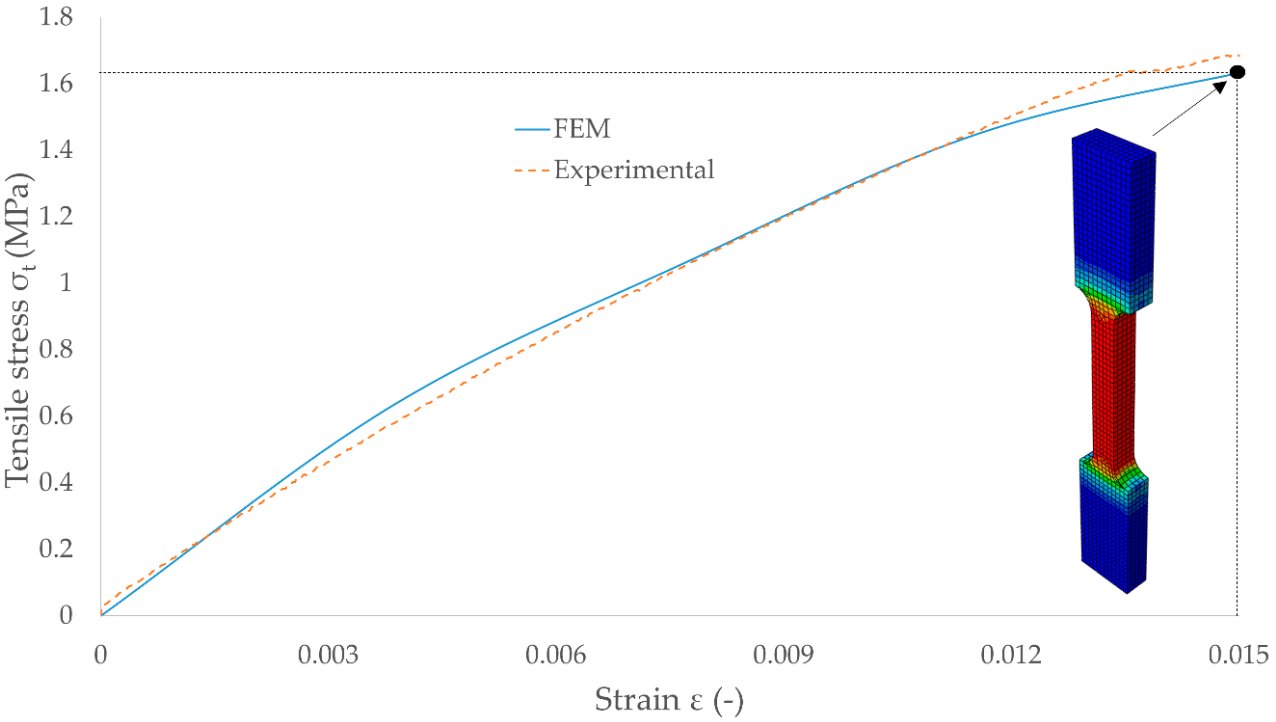

Figure 20. Characteristics of pine wood (*Pinus L.* Sp. Pl. 1000. 1753) with 19.9% moisture content in the tangential direction (T) tensile test obtained from the FEM analysis and compared with the averaged experimental result.

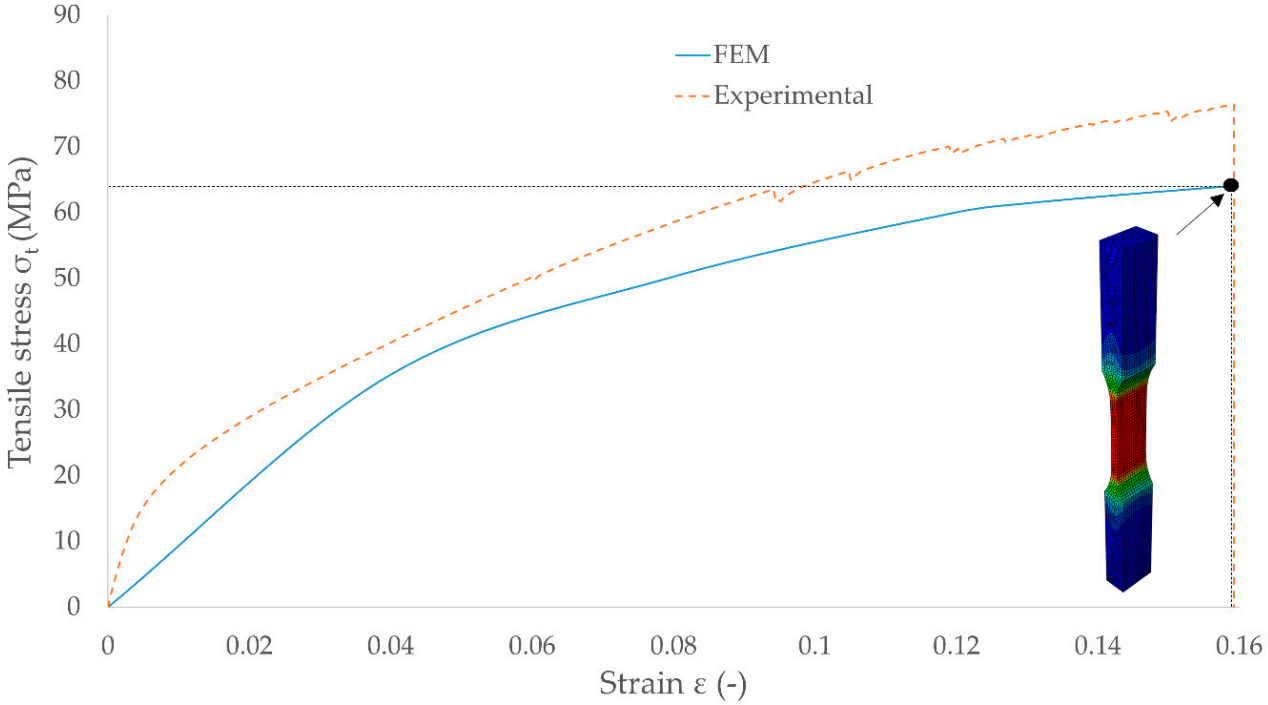

Figure 21. Characteristics of pine wood (*Pinus L.* Sp. Pl. 1000. 1753) with 8.74% moisture content in the longitudinal direction (L) during tensile test obtained from the FEM analysis and compared with the averaged experimental result.

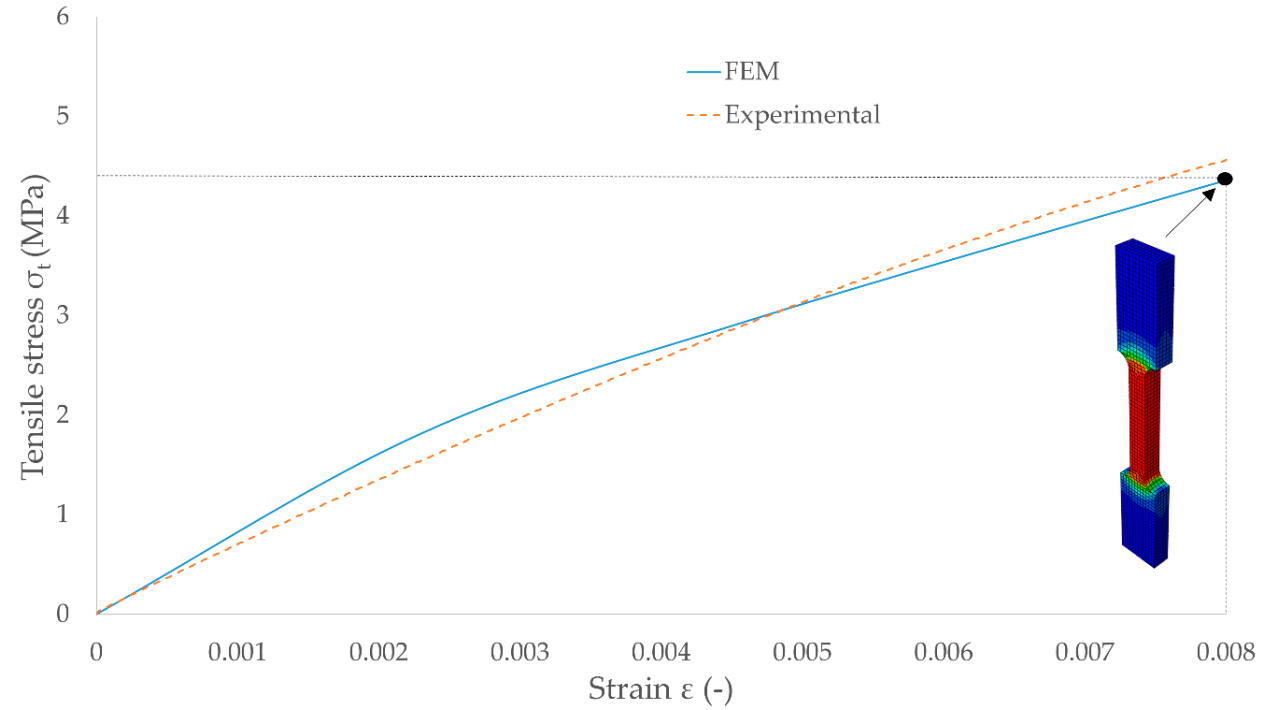

Figure 22. Characteristics of pine wood (*Pinus L.* Sp. Pl. 1000. 1753) with 8.74% moisture content in the radial direction (R) during tensile test obtained from the FEM analysis and compared with the averaged experimental result.

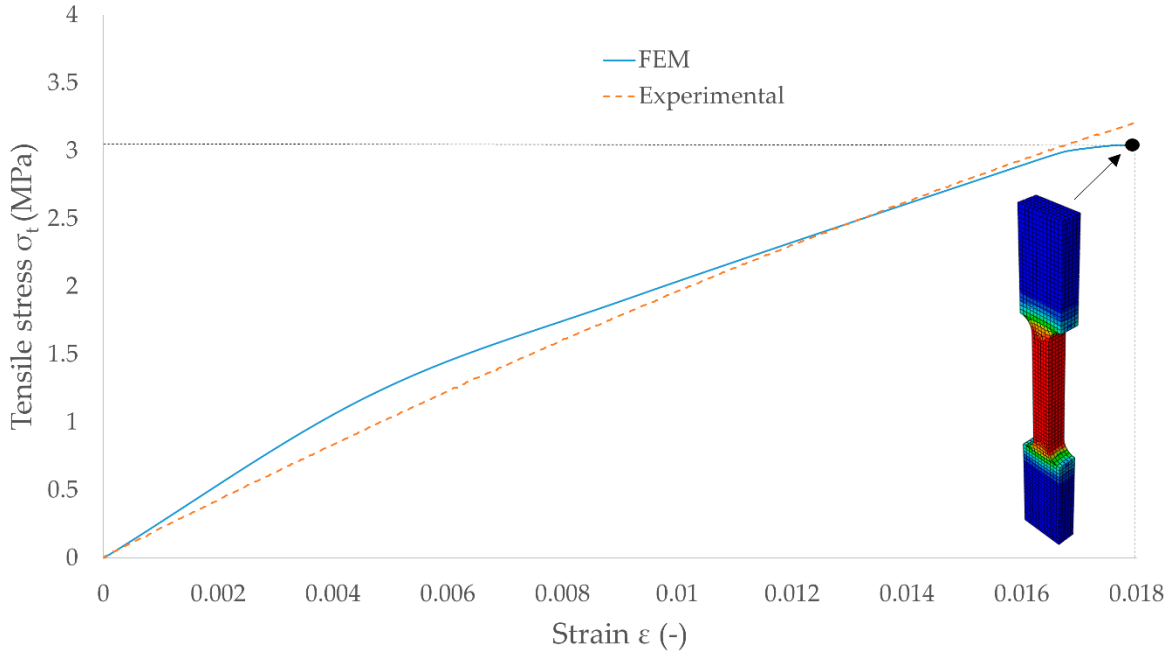

Figure 23. Characteristics of pine wood (*Pinus L.* Sp. Pl. 1000. 1753) with 8.74% moisture content in the tangential direction (T) during tensile test obtained from the FEM analysis and compared with the averaged experimental result.

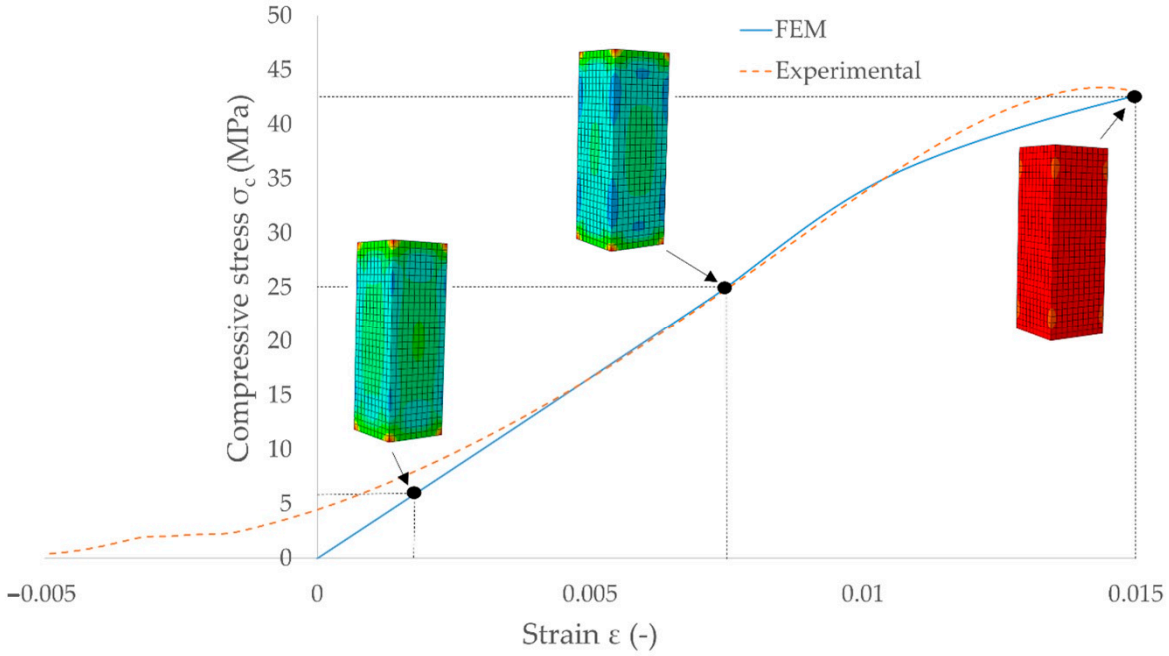

Figure 24. Characteristics of pine wood (*Pinus L.* Sp. Pl. 1000. 1753) with 19.9% moisture content in the longitudinal direction (L) during compression obtained from the FEM analysis and compared with the averaged experimental result.

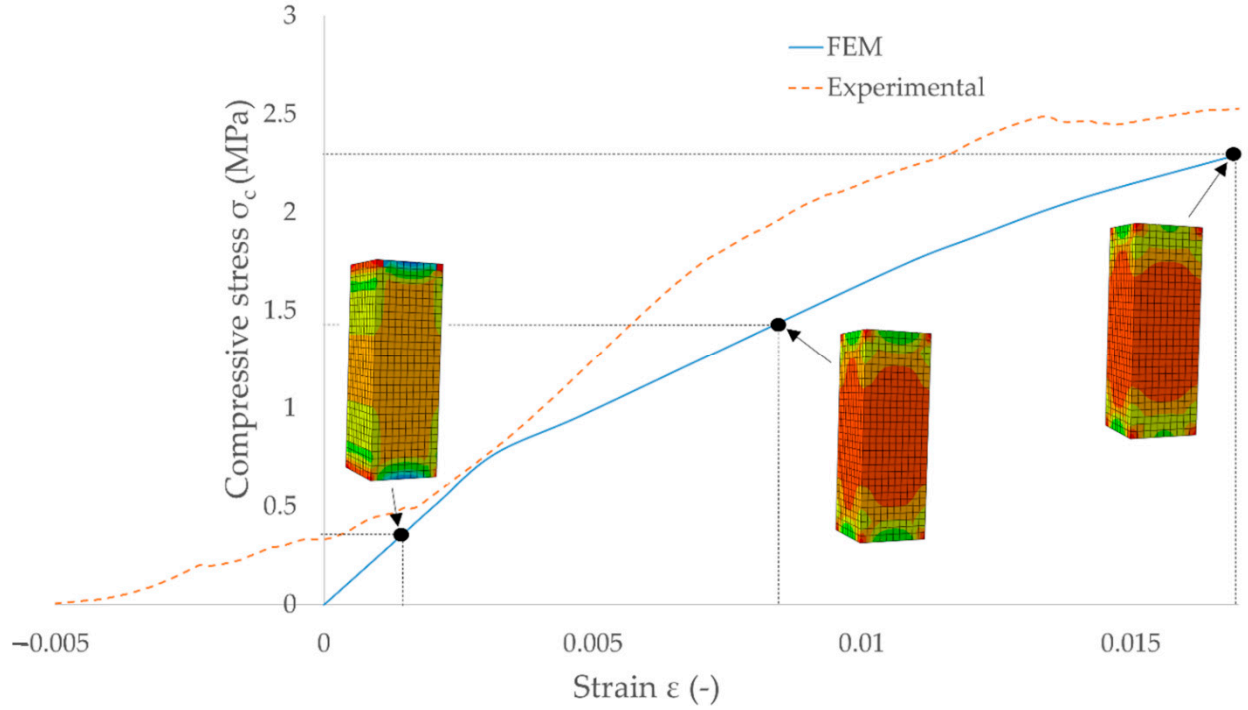

Figure 25. Characteristics of pine wood (*Pinus L.* Sp. Pl. 1000. 1753) with 19.9% moisture content in the radial direction (R) during compression obtained from the FEM analysis and compared with the averaged experimental result.

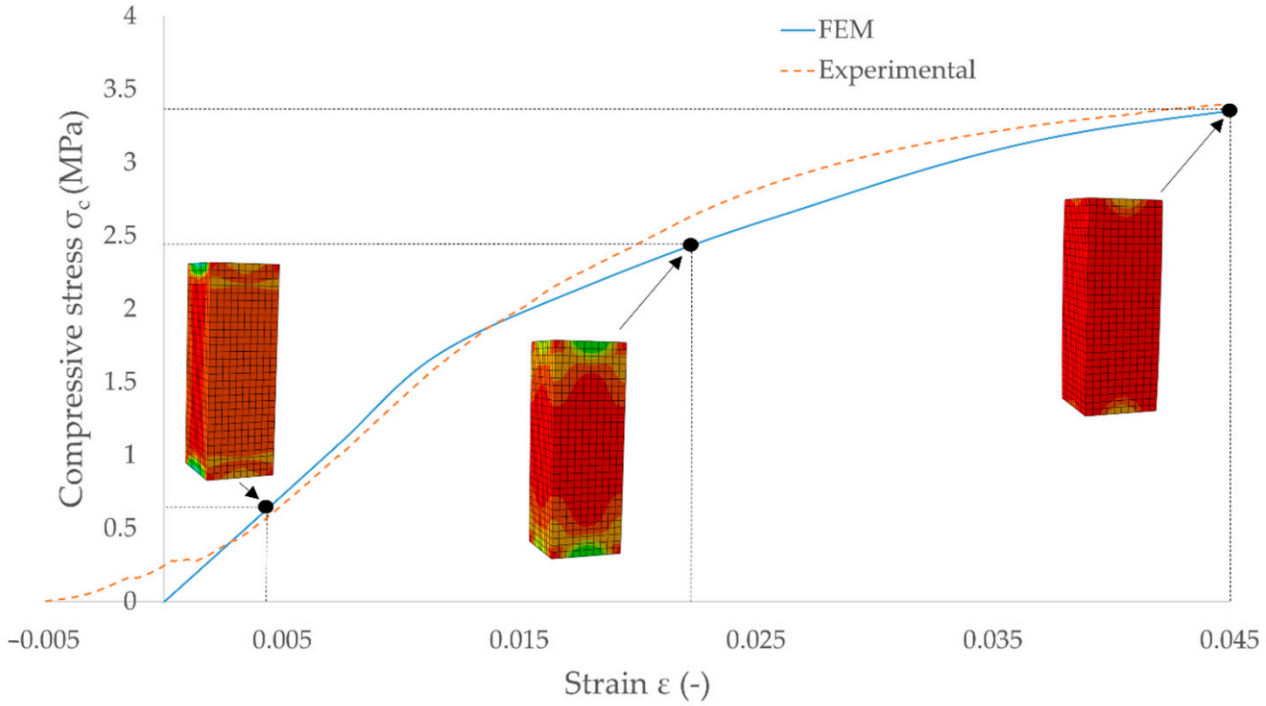

Figure 26. Characteristics of pine wood (*Pinus L.* Sp. Pl. 1000. 1753) with 19.9% moisture content in the tangential direction (T) during compression obtained from the FEM analysis and compared with the averaged experimental result.

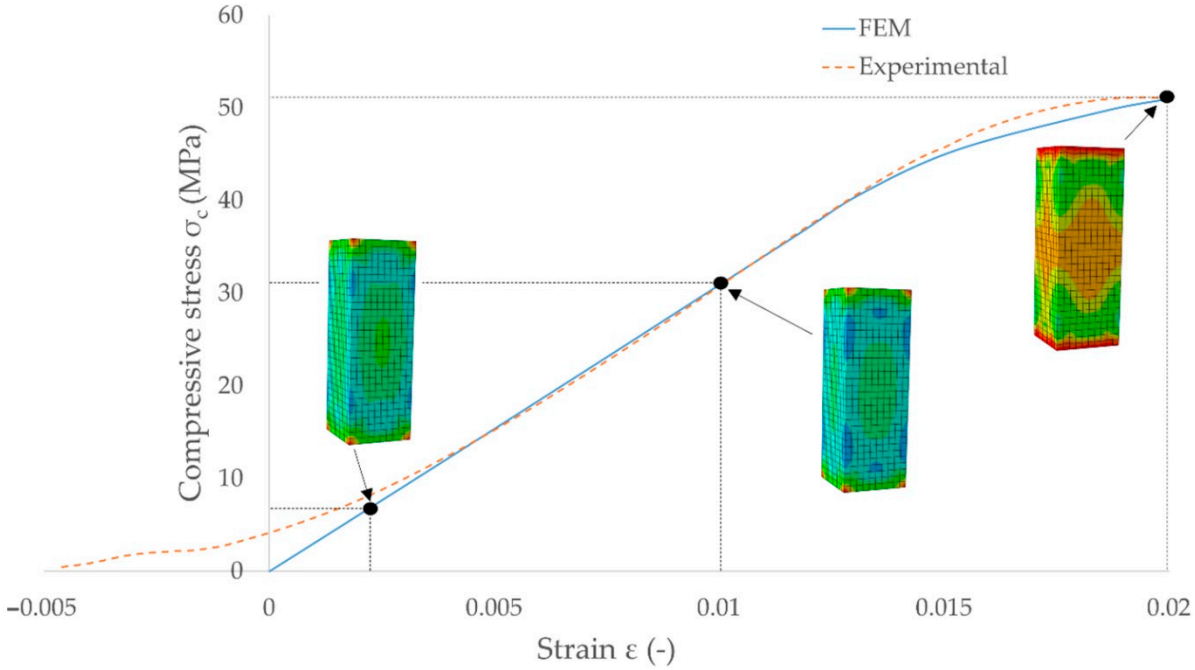

Figure 27. Characteristics of pine wood (*Pinus L.* Sp. Pl. 1000. 1753) with 8.74% moisture content in the longitudinal direction (L) during compression obtained from the FEM analysis and compared with the averaged experimental result.

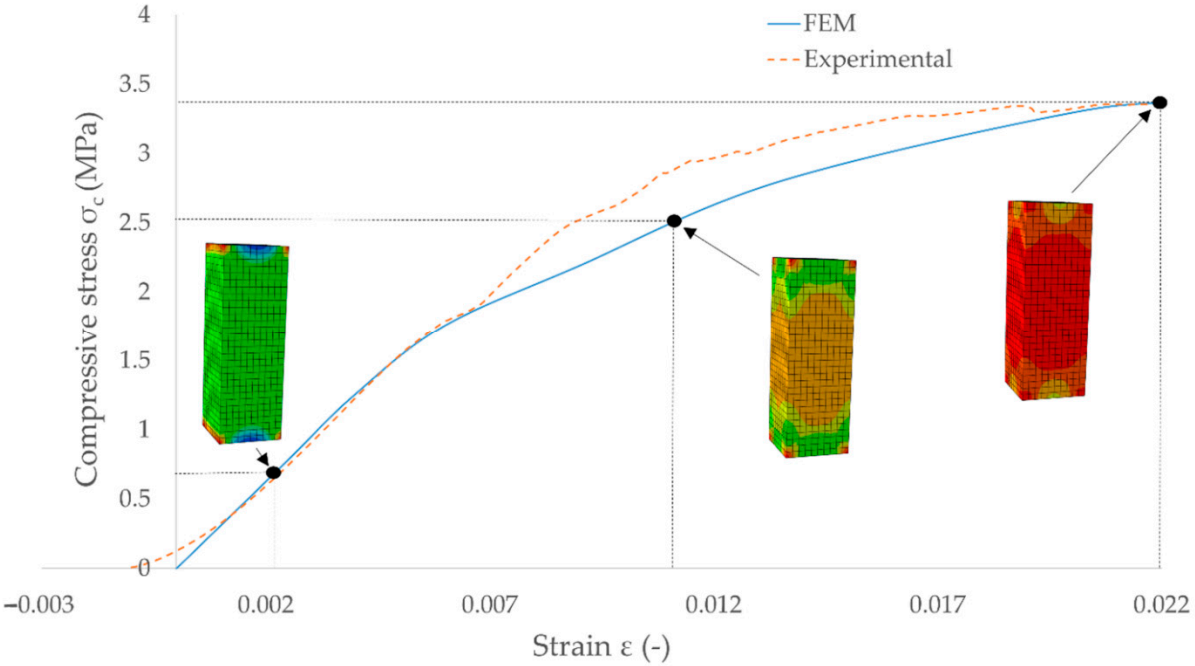

Figure 28. Characteristics of pine wood (*Pinus L.* Sp. Pl. 1000. 1753) with 8.74% moisture content in the radial direction (R) during compression obtained from the FEM analysis and compared with the averaged experimental result.

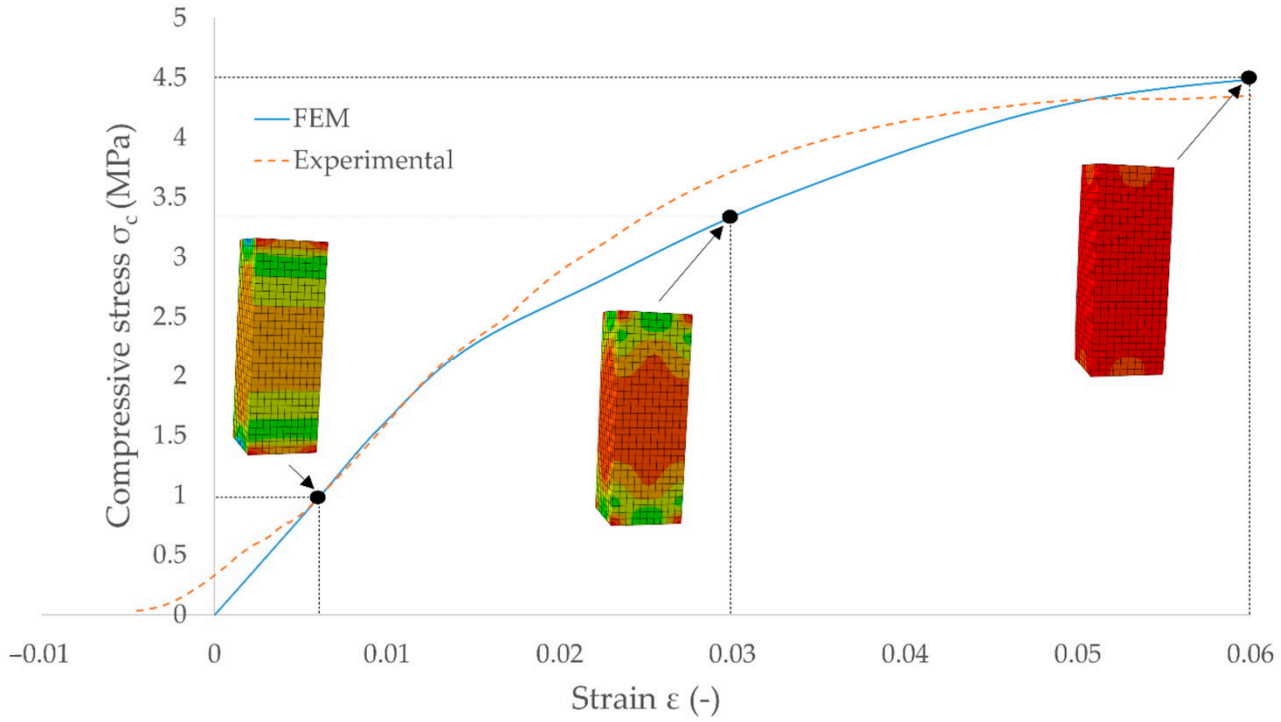

Figure 29. Characteristics of pine wood (*Pinus L.* Sp. Pl. 1000. 1753) with 8.74% moisture content in the tangential direction (T) during compression obtained from the FEM analysis and compared with the averaged experimental result.

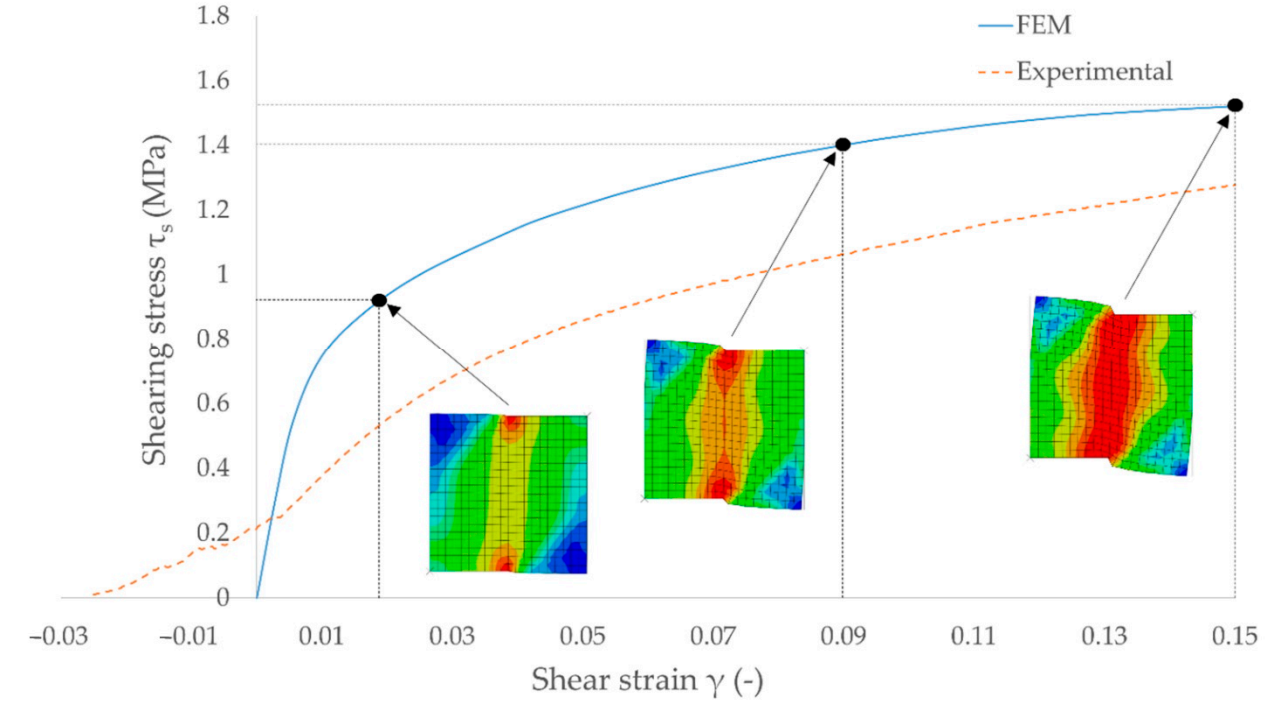

Figure 30. Characteristics of pine wood (*Pinus L.* Sp. Pl. 1000. 1753) with 19.9% moisture content crosswise to the fibers in the radial plane (RT) during shear obtained from the FEM analysis and compared with the averaged experimental result.

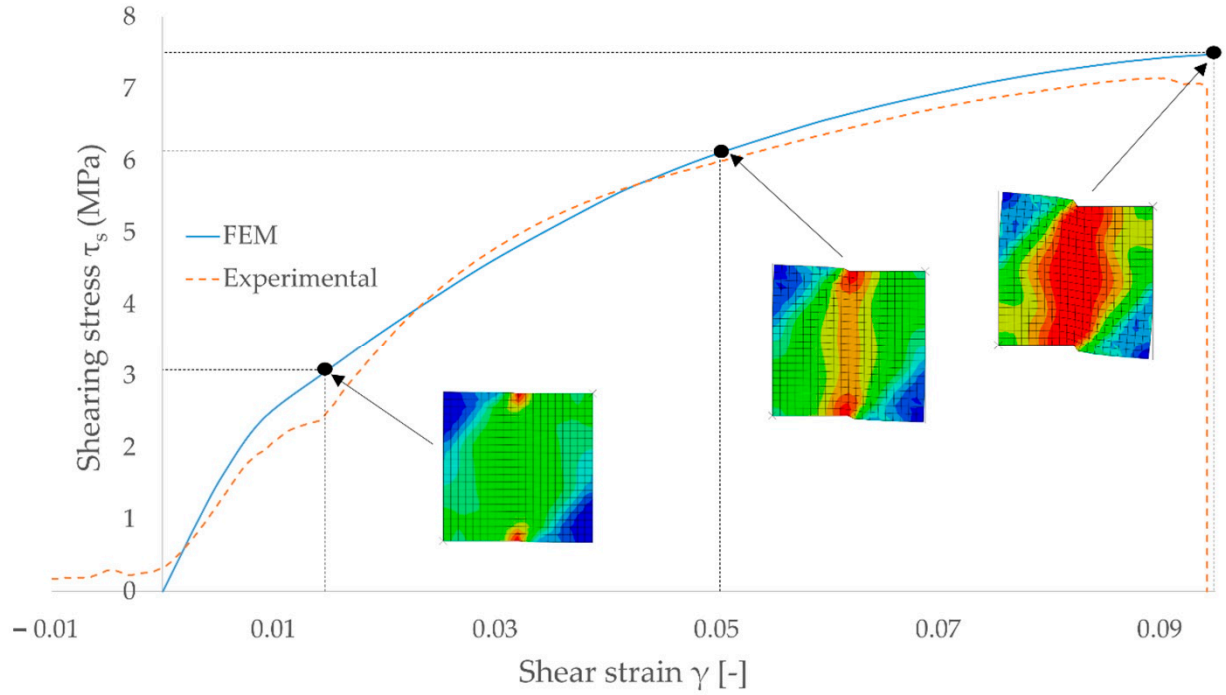

Figure 31. Characteristics of pine wood (*Pinus L.* Sp. Pl. 1000. 1753) with 19.9% moisture content in the direction along the fibers in the radial plane (LR) during shear obtained from the FEM analysis and compared with the averaged experimental result.

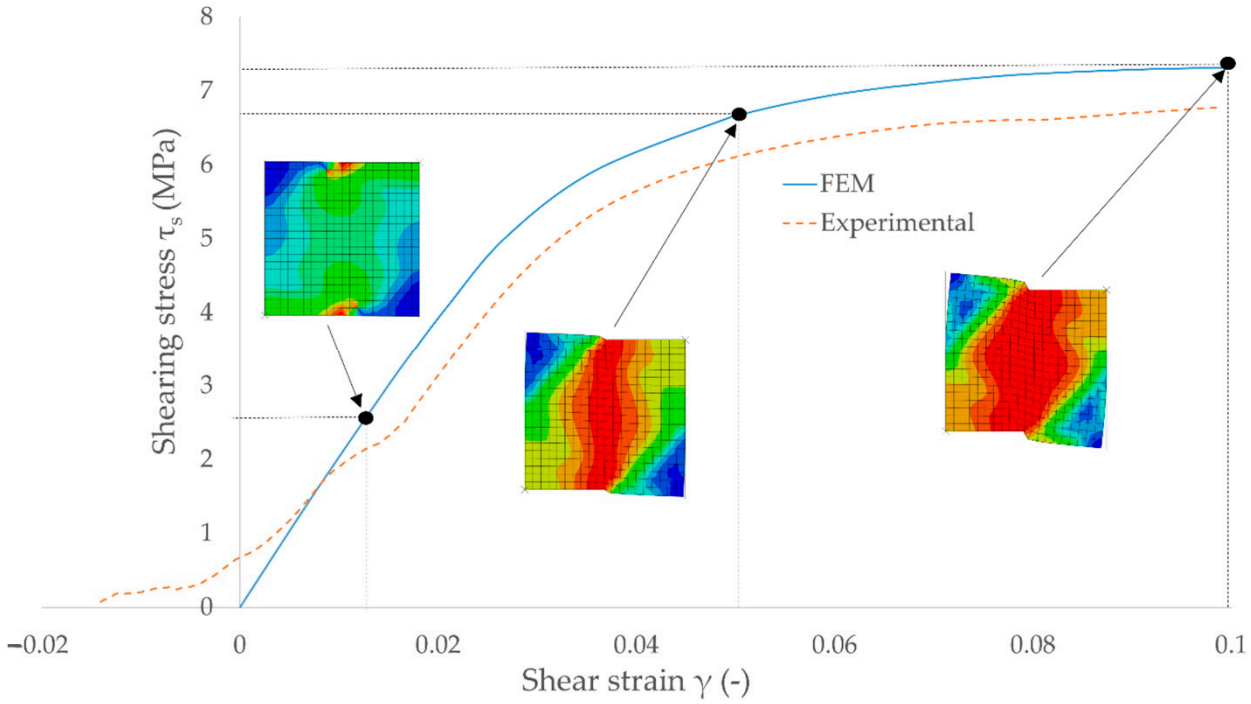

Figure 32. Characteristics of pine wood (Pinus L. Sp. Pl. 1000. 1753) with 19.9% moisture content in the direction along the fibers in the tangential plane (LT) during shear obtained from the FEM analysis and compared with the averaged experimental result.

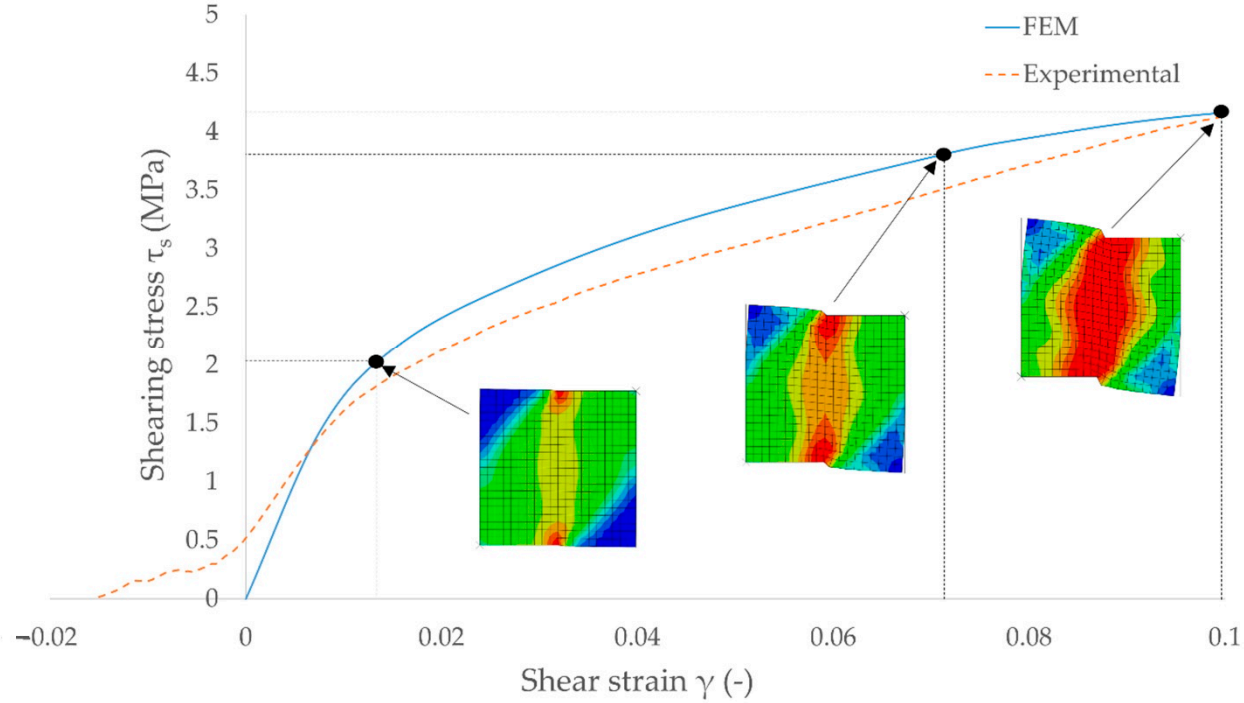

Figure 33. Characteristics of pine wood (*Pinus L.* Sp. Pl. 1000. 1753) with 8.74% moisture content crosswise to the fibers in the radial plane (RT) during shear obtained from the FEM analysis and compared with the averaged experimental result.

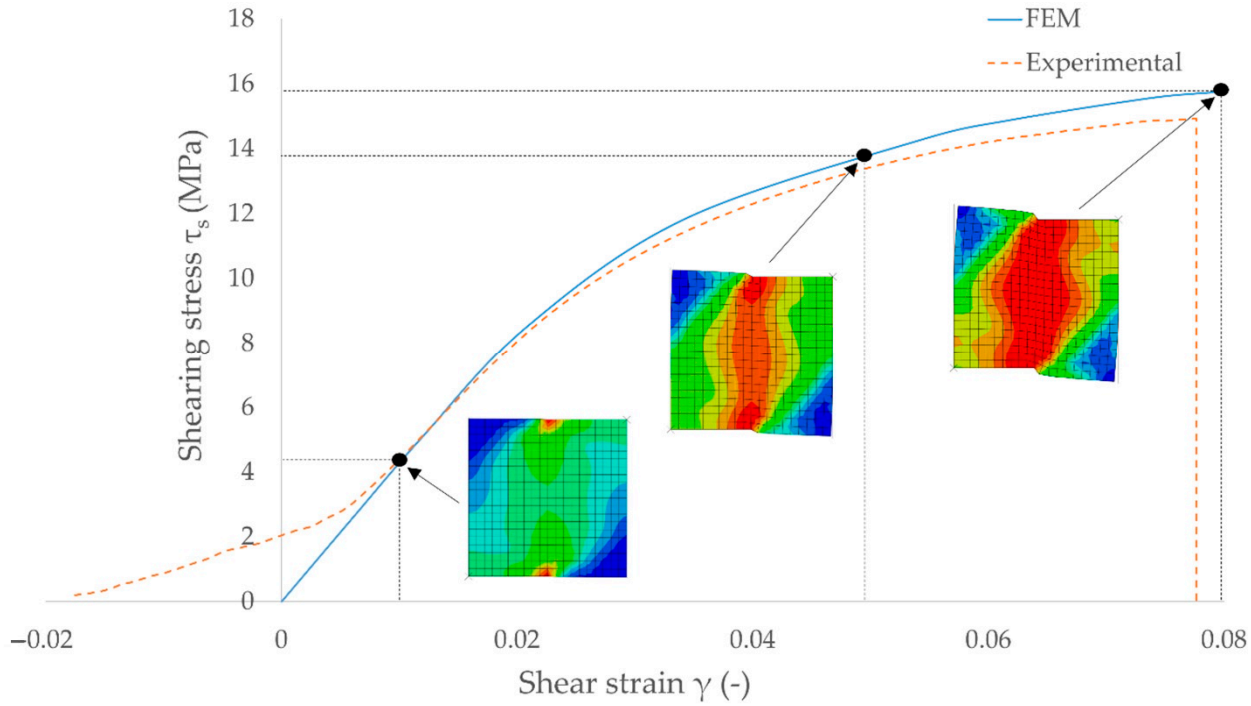

Figure 34. Characteristics of pine wood (*Pinus L.* Sp. Pl. 1000. 1753) with 8.74% moisture content in the direction along the fibers in the radial plane (LR) during shear obtained from the FEM analysis and compared with the averaged experimental result.

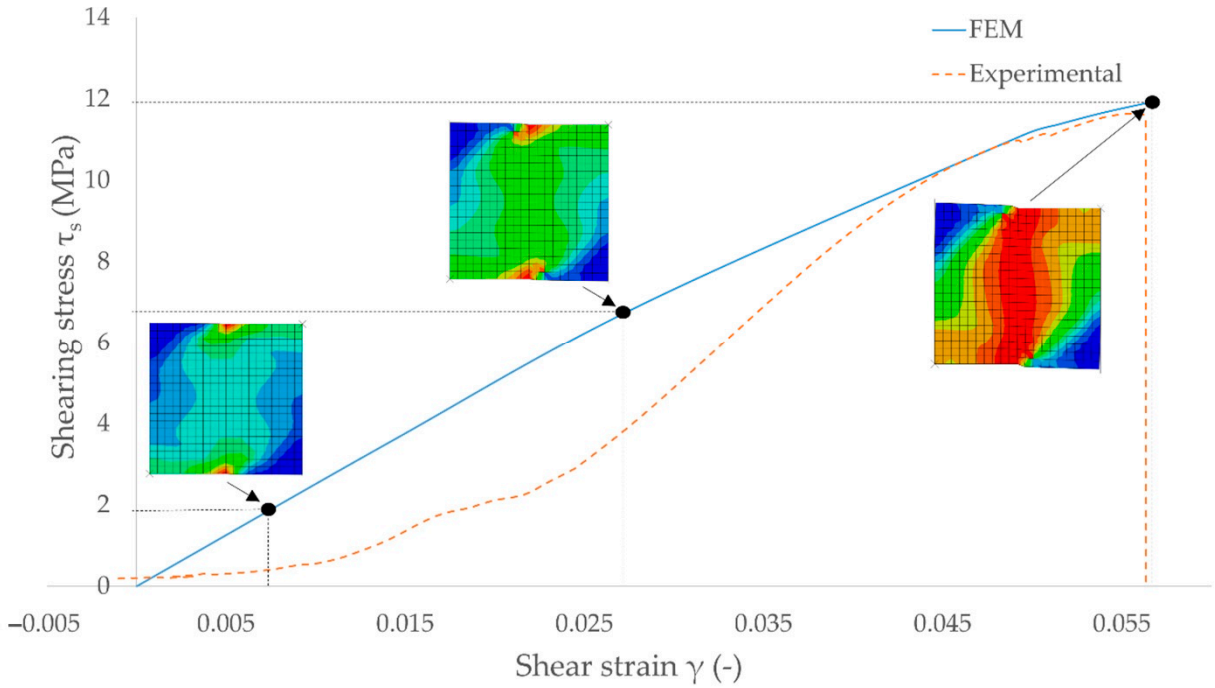

Figure 35. Characteristics of pine wood (*Pinus L.* Sp. Pl. 1000. 1753) with 8.74% moisture content in the direction along the fibers in the tangential plane (LT) during shear obtained from the FEM analysis and compared with the averaged experimental result.

Table 7. Comparison of model convergence with strength tests during tensile testing at the point of damage; L—longitudinal direction, R—radial direction, T—tangential direction.

Direction	L		R		T	
Moisture content [%]	8.74	19.9	8.74	19.9	8.74	19.9
FEM model [MPa]	64	41	4.38	3.48	3.27	1.68
Strength tests [MPA]	76	74	4.98	3.57	3.04	1.65
Error [%]	16	44	12	2.5	7.5	2

Table 8. Comparison of model convergence with strength tests during compression test at the point of damage; L—longitudinal direction, R—radial direction, T—tangential direction.

Direction	L		R		T	
Moisture content [%]	8.74	19.9	8.74	19.9	8.74	19.9
FEM model [MPa]	51	44	3.4	2.4	4.6	3.6
Strength tests [MPA]	51	43.5	3.4	2.5	4.4	3.4
Error [%]	0	1	0	4	4.5	5.5

Table 9. Comparison of model convergence with strength tests during the shear testing at the point of damage; crosswise to the fibers in the radial plane (RT), along the fibers in the radial plane (LR), along the fibers in the tangential plane (LT).

Direction	RT		LR		LT	
Moisture content [%]	8.74	19.9	8.74	19.9	8.74	19.9
FEM model [MPa]	4.3	1.5	16	7.5	11.9	7.4
Strength tests [MPA]	4.1	1.3	15	7.1	11.6	6.8
Error [%]	5	13	6	5	3	8

Table 10. Comparison of the convergence characteristics of the model with the strength tests during the tensile test; L—longitudinal direction, R—radial direction, T—tangential direction.

Direction	L		R		T	
Moisture content [%]	8.74	19.9	8.74	19.9	8.74	19.9
Error 15% [%]	25	31	100	100	100	100

Table 11. Comparison of the convergence characteristics of the model with the strength tests during the compression test; L—longitudinal direction, R—radial direction, T—tangential direction.

Direction	L		R		T	
Moisture Content [%]	8.74	19.9	8.74	19.9	8.74	19.9
Error 15% [%]	95	94	100	22	96	97

Table 12. Comparison of the convergence characteristics of the model with the strength tests during the shear test; crosswise to the fibers in the radial plane (RT), along the fibers in the radial plane (LR), along the fibers in the tangential plane (LT).

Direction	RT		LR		LT	
Moisture Content [%]	8.74	19.9	8.74	19.9	8.74	19.9
Error 15% [%]	94	5	96	99	51	85

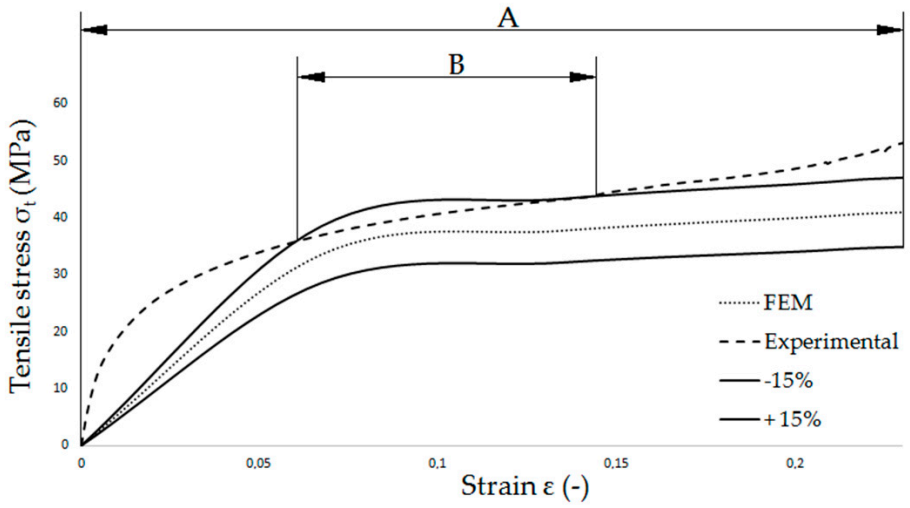

Figure 36. Example characteristics showing the methodology of covering the characteristics of the FEM model with the characteristics determined during the strength tests, where: A—the length of the characteristics from the strength test, B—the length of the sections of the FEM model characteristics (±15%) overlapping with the characteristics of the strength tests.

The error of the maximum value of the destructive force determined by the FEM analysis, estimated as the arithmetic mean of the errors obtained for each analyzed case, is 8%, and the median average for these results equals 5%. The error value is in the range from 0% to 44%. The average error value in selected strength tests equals 14% for tensile, 2.5% for compression, 6.5% for shear. In contrast, the average coverage of the FEM characteristics with the results of tests from the strength test in the field of elastic-plastic deformations with the assumed ±15% error overlap with the average of around 77% arithmetically, and the median for these results equals 95.5%. The average coverage of the characteristics in selected strength tests equals 76% for tensile, 84% for compressive, 72% for shear.

5.3. Aspects of Symmetry in the Tested Samples

The symmetrical nature of the stress distribution is clearly visible on simulation models. The nature of damage in tested samples presented in Figure 37 for tensile and Figure 38 for shear shows the convergent nature of the influence of the forces. In the samples subjected to compression, the influence of the forces is hardly noticeable, therefore it has not been presented. A similar nature of the stress distribution in tested materials samples is available, for example, for composite materials [83], steel [84], wood [28,85]. Additionally, the symmetrical stress distribution is noticeable in the tested structures, e.g., frames of: road bridges [86], bicycles [87], vehicles [88], bridges [89] or machine parts: gears [90,91], turbine blades [92], and furniture connections [93].

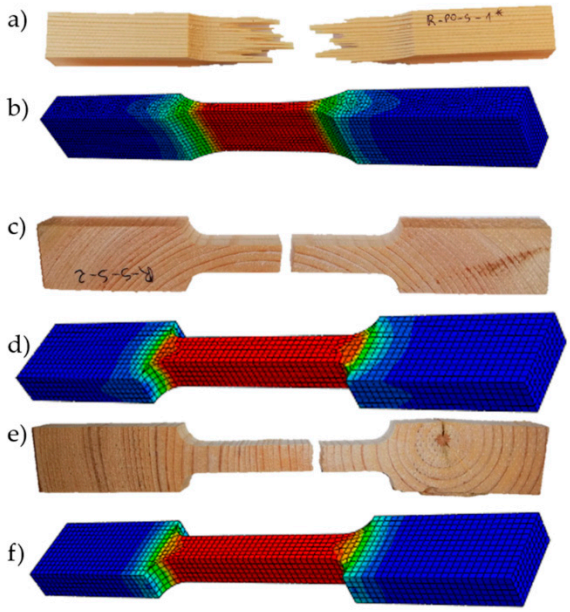

Figure 37. Pine wood samples with a moisture content of 8.74% destroyed during the tensile test compared to the stress distribution in the simulation model, where: samples in the longitudinal direction (L) (**a**) real, (**b**) 3D model in the radial direction (R) (**c**) real, (**d**) 3D model; in the tangential direction (T) (**e**) real, (**f**) 3D model.

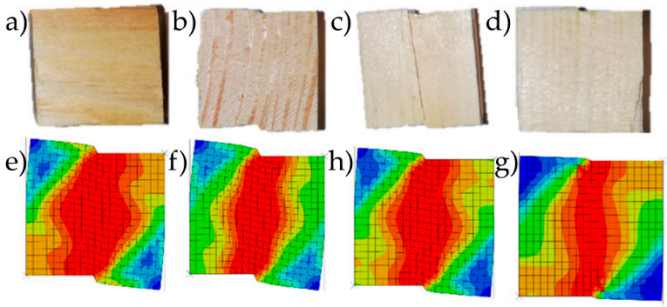

Figure 38. Pine wood samples with a moisture content of 8.74% destroyed during the shear test compared with the stress distribution in the simulation model, where: real samples: (**a**) crosswise to the fibers in the tangential plane (TR), (**b**) crosswise to the fibers in the radial plane (RT), (**c**) along the fibers in the radial plane (LR), (**d**) along the fibers in the tangential plane (LT); model 3D: (**e**) crosswise to the fibers in the tangential plane (TR), (**f**) crosswise to the fibers in the radial plane (RT), (**g**) along the fibers in the radial plane (LR), (**h**) along the fibers in the tangential plane (LT).

6. Conclusions

Mathematical models that enable the prediction of destructive force value of the tested samples in various stress states (compression, shear, and tension), allow for a more accurate prediction of the effects of forces acting on the tested material. In industrial applications, such models can be used to determine cutting force during chipping processes described in the modern trend of modeling cutting force using FEM analysis [94–97]. This will contribute to the development of efficient and ecological machines.

Conducting research with the use of the developed numerical model enables prediction of values with quite high accuracy. This is guaranteed by the presented comparison with the results of experimental tests. The recorded convergence in the estimation of the strength parameters of wood processing is at the level of about 8%.

Research confirms that wood with lower moisture content is characterized by greater durability in most strength tests. This indicates that it is more advantageous to carry out the chipping processes of untreated wood.

The geometry of the samples used in the tests and the simplifications in the model, mainly based on the assumption of a homogeneous material in the entire cross-section of the sample, contribute to the symmetrical nature of the stress distribution in real and numerical samples.

Author Contributions: Conceptualization, Ł.W., D.W.; methodology, Ł.W., D.W. and M.K. software, D.W. and Ł.W.; validation, Ł.W., D.W., M.K. and K.T.; formal analysis, D.W., Ł.W. and K.T.; investigation, Ł.W., M.K., D.W. and K.T.; resources, Ł.W. and D.W.; data curation, Ł.W., M.K. and D.W.; writing—original draft preparation, Ł.W., M.K. and D.W.; writing—review and editing, M.K., D.W., K.T. and Ł.W.; visualization, D.W., Ł.W. and M.K.; supervision, Ł.W., K.T.; project administration, Ł.W.; funding acquisition, Ł.W. All authors have read and agreed to the published version of the manuscript.

Funding: Research was performed as part of the project "Interdisciplinary Dean's Grant (IDG) of Poznań University of Technology" determined in the year 2020 for the subject—air quality in Poznań and how to improve it. Project title: "Design and research of mobile machines chipping wastes from urban agriculture processes for innovative construction solutions limiting the impact on the natural environment and machine operators" (33/32/SIGR/3334) financed by the Poznan University of Technology.

Conflicts of Interest: The authors declare no conflict of interest.

References

1. Frumkin, H. Beyond toxicity: Human health and the natural environment. *Am. J. Prev. Med.* **2001**, *20*, 234–240. [CrossRef]
2. Baró, F.; Chaparro, L.; Baggethun, E.G.; Langemeyer, J.; Nowak, D.J.; Terradas, J. Contribution of ecosystem services to air quality and climate change mitigation policies: The case of urban forests in Barcelona, Spain. *Ambio* **2014**, *43*, 466–479. [CrossRef] [PubMed]
3. Mullaney, J.; Lucke, T.; Trueman, S.J. A review of benefits and challenges in growing street trees in paved urban environments. *Landsc. Urban Plan.* **2015**, *134*, 157–166. [CrossRef]
4. Selmi, W.; Weber, C.; Rivière, E.; Blond, N.; Mehdi, L.; Nowak, D. Air pollution removal by trees in public green spaces in Strasbourg city, France. *Urban For. Urban Green.* **2016**, *17*, 192–201. [CrossRef]
5. Song, C.; Lee, W.K.; Choi, H.A.; Kim, J.; Jeon, S.W.; Kim, J.S. Spatial assessment of ecosystem functions and services for air purification of forests in South Korea. *Environ. Sci. Policy* **2016**, *63*, 27–34. [CrossRef]
6. Sawidis, T.; Breuste, J.; Mitrovic, M.; Pavlovic, P.; Tsigaridas, K. Trees as bioindicator of heavy metal pollution in three European cities. *Environ. Pollut.* **2011**, *159*, 3560–3570. [CrossRef]
7. Prada, M.; Alonso, C.M.; García, S.S.; Canga, E. Analysis of three forest chippers: Productivity, costs and GHG emissions in Northern Spain. *J. Clean. Prod.* **2015**, *101*, 238–244. [CrossRef]
8. Manzone, M. Energy consumption and CO_2 analysis of different types of chippers used in wood biomass plantations. *Appl. Energy* **2015**, *156*, 686–692. [CrossRef]
9. Niinikoski, J.; Ewalds, J.; Heikkinen, E.; Kotilainen, J.; Kääriäinen, M.; Tammi, K.; Kiviluoma, P.; Korhonen, A.; Kuosmanen, P. Methods for reducing emissions of small internal combustion engines. In Proceedings of the 11th International DAAAM Baltic Conference, Industrial Engineering, Tallinn, Estonia, 20–22 April 2016.
10. Warguła, Ł.; Krawiec, P.; Waluś, K.J.; Kukla, M. Fuel Consumption Test Results for a Self-Adaptive, Maintenance-Free Wood Chipper Drive Control System. *Appl. Sci.* **2020**, *10*, 2727. [CrossRef]

11. Szpica, D. Coefficient of engine flexibility as a basis for the assessment of vehicle tractive performance. *Chin. J. Mech. Eng.* **2019**, *32*, 9. [CrossRef]
12. Szpica, D.; Czaban, J. Operational assessment of selected gasoline and LPG vapour injector dosage regularity. *Mechanika* **2014**, *20*, 480–489. [CrossRef]
13. Li, L.; Liu, Z.; Wang, H.; Deng, B.; Wang, Z.; Xiao, Z.; Su, Y.; Jiang, B. Development of a gas-phase LPG injection system for a small SI engine. *SAE Technol. Pap.* **2003**, 1–9. [CrossRef]
14. Patil, C.; Varade, S.; Wadkar, S. A review of engine downsizing and its effects. *Int. J. Curr. Eng. Technol.* **2017**, *7*, 319–324.
15. Warguła, Ł.; Adamiec, J.M.; Waluś, K.J.; Krawiec, P. The Characteristics Analysis of Torque and Rotation Speed of Working Unit of Branch Grinder-Introductory Research. In Proceedings of the MATECWeb of Conferences, Proceedings of the Machine Modelling and Simulations, Sklené Teplice, Slovak Republic, 5–8 September 2017; Volume 157.
16. Warguła, Ł.; Krawiec, P. The research on the characteristic of the cutting force while chipping of the Caucasian Fir (*Abies nordmanniana*) with a single-shaft wood chipper. *IOP Conf. Ser. Mater. Sci. Eng.* **2020**, *776*, 012012. [CrossRef]
17. Macko, M.; Tyszczuk, K.; Śmigielski, G.; Mroziński, A. Utility of an Unitary-Shredding Method to Evaluate the Conditions and Selection of Constructional Features during Grinding. In Proceedings of the MATECWeb of Conferences, Proceedings of the Machine Modelling and Simulations, Sklené Teplice, Slovak Republic, 5–8 September 2017; Volume 157.
18. Macko, M.; Tyszczuk, K.; Śmigielski, G.; Flizikowski, J.; Mroziński, A. The Use of CAD Applications in the Design of Shredders for Polymers. In Proceedings of the MATECWeb of Conferences, Proceedings of the Machine Modelling and Simulations, Sklené Teplice, Slovak Republic, 5–8 September 2017; Volume 157.
19. Kaygin, B.; Yorur, H.; Uysal, B. Simulating Strength Behaviors of Corner Joints of Wood Constructions by Using Finite Element Method. *Wood Ind. Drv. Ind.* **2016**, *67*, 133–140. [CrossRef]
20. Ilic, S.; Hackl, K. Application of the multiscale FEM to the modeling of nonlinear multiphase materials. *J. Theor. Appl. Mech.* **2009**, *47*, 537–551.
21. Jeong, G.Y.; Hindman, D.P. Modeling differently oriented loblolly pine strands incorporating variation of intraring properties using a stochastic finite element method. *Wood Fiber Sci.* **2010**, *42*, 51–61.
22. Pétrissans, A.; Hamada, J.; Chaouch, M.; Petrissans, M.; Gerardin, P. Modeling and numerical simulation of wood torrefaction. *Innov. Woodwork. Ind. Eng. Des.* **2015**, *5*, 26–32.
23. Hansson, L.; Lundgren, N.; Antti, A.L.; Hagman, O. Finite element modeling (FEM) simulation of interactions between wood and microwaves. *J. Wood Sci.* **2006**, *52*, 406–410. [CrossRef]
24. Staneva, N.; Genchev, Y.; Hristodorova, D. FEM analysis of deformations and stresses of upholstered furniture skeleton made of scots pine and OSB. *Int. J. Wood Des. Technol.* **2017**, *6*, 31–37.
25. Tankut, N.; Tankut, A.N.; Zor, M. Finite element analysis of wood materials. *Drv. Ind. Znan. Casopis Pitanja Drv. Tehnol.* **2014**, *65*, 159–171. [CrossRef]
26. Kurata, Y. A Comparison of the Loading Direction for Bending Strength with Different Wood Measurement Surfaces Using Near-Infrared Spectroscopy. *Forests* **2020**, *11*, 644. [CrossRef]
27. Fajdiga, G.; Rajh, D.; Nečemer, B.; Glodež, S.; Šraml, M. Experimental and Numerical Determination of the Mechanical Properties of Spruce Wood. *Forests* **2019**, *10*, 1140. [CrossRef]
28. Hu, W.; Wan, H.; Guan, H. Size Effect on the Elastic Mechanical Properties of Beech and Its Application in Finite Element Analysis of Wood Structures. *Forests* **2019**, *10*, 783. [CrossRef]
29. Kawecki, B.; Podgórski, J. 3D Abaqus Simulation of Bent Softwood Elements. *Arch. Civ. Eng.* **2020**, *3*, 323–337.
30. Malujda, I.; Talaśka, K. Identification of phenomena accompanying the process of compressing natural polymers. *Procedia Eng.* **2017**, *177*, 369–374. [CrossRef]
31. Mania, P.; Siuda, F.; Roszyk, E. Effect of Slope Grain on Mechanical Properties of Different Wood Species. *Materials* **2020**, *13*, 1503. [CrossRef]
32. Mohammadabadi, M.; Jarvis, J.; Yadama, V.; Cofer, W. Predictive Models for Elastic Bending Behavior of a Wood Composite Sandwich Panel. *Forests* **2020**, *11*, 624. [CrossRef]
33. Yan, W.; Fu, W.; Zhang, B.; Zhou, J. Hygrothermal Effect on Axial Compressive Properties of Bionic Bamboo Element. *Wood Res.* **2020**, *65*, 37–50. [CrossRef]
34. Beery, W.H.; Ifju, G.; McLain, T.E. Quantitative wood anatomy—Relating anatomy to transverse tensile strength. *Wood Fiber Sci.* **2007**, *15*, 395–407.
35. Bahmani, M.; Fathi, L.; Koch, G.; Kool, F.; Aghajani, H.; Humar, M. Heartwood and Sapwood Features Of Sorbus Torminalis Grown in Iranian Forests. *Wood Res.* **2020**, *65*, 195–204. [CrossRef]
36. Dudík, R.; Borůvka, V.; Zeidler, A.; Holeček, T.; Riedl, M. Influence of Site Conditions and Quality of Birch Wood on Its Properties and Utilization after Heat Treatment. Part II—Surface Properties and Marketing Evaluation of the Effect of the Treatment on Final Usage of Such Wood. *Forests* **2020**, *11*, 556. [CrossRef]
37. Chuchała, D.; Orłowski, K.; Ochrymiuk, T. The forecasted values of cutting power for sawing on band sawing machines for Polish Scots pine wood (*Pinus sylvestris* L.) in a function of its provenance. *Ann. WULS For. Wood Technol.* **2017**, *99*, 81–87.
38. Tomczak, K.; Tomczak, A.; Jelonek, T. Effect of Natural Drying Methods on Moisture Content and Mass Change of Scots Pine Roundwood. *Forests* **2020**, *11*, 668. [CrossRef]

39. Taghiyari, H.R.; Bayani, S.; Militz, H.; Papadopoulos, A.N. Heat Treatment of Pine Wood: Possible Effect of Impregnation with Silver Nanosuspension. *Forests* **2020**, *11*, 466. [CrossRef]
40. Bal, B.C. A comparative study of some of the mechanical properties of pine wood heat treated in vacuum, nitrogen, and air atmospheres. *BioResources* **2018**, *13*, 5504–5511.
41. Mannaa, M.; Han, G.; Jeon, H.W.; Kim, J.; Kim, N.; Park, A.R.; Kim, J.-C.; Seo, Y.-S. Influence of Resistance-Inducing Chemical Elicitors against Pine Wilt Disease on the Rhizosphere Microbiome. *Microorganisms* **2020**, *8*, 884. [CrossRef]
42. Khanova, E.; Konovalov, V.; Timeryanov, A.; Isyanyulova, R.; Rafikova, D. Genetic and Selection Assessment of The Scots Pine (*Pinus Sylvestris* L.) In Forest Seed Orchards. *Wood Res.* **2020**, *65*, 283–292. [CrossRef]
43. Özgüven, F.; Vursavuş, K. Some physical, mechanical and aerodynamic properties of pine (*Pinus pinea*) nuts. *J. Food Eng.* **2005**, *68*, 191–196.
44. Esteves, B.; Marques, A.V.; Domingos, I.; Pereira, H. Influence of steam heating on the properties of pine (*Pinus pinaster*) and eucalypt (*Eucalyptus globulus*) wood. *Sci. Technol.* **2007**, *41*, 193. [CrossRef]
45. Grazide, C.; Coureau, J.L.; Cointe, A.; Morel, S. Mechanical performance curves for the strength grading of maritime pine. *Eur. J. Wood Wood Prod.* **2018**, *76*, 877–888. [CrossRef]
46. Groom, L.H.; Mott, L.; Shaler, S. Mechanical properties of individual southern pine fibers. Part I. Determination of variability of stress-strain curves with respect to tree height and juvenility. *Wood Fiber Sci.* **2002**, *34*, 14–27.
47. Singha, A.S.; Thakur, V.K. Mechanical, morphological and thermal properties of pine needle-reinforced polymer composites. *Int. J. Polym. Mater.* **2008**, *58*, 21–31. [CrossRef]
48. Orlowski, K.A.; Ochrymiuk, T.; Atkins, A.; Chuchala, D. Application of fracture mechanics for energetic effects predictions while wood sawing. *Wood Sci. Tech.* **2013**, *47*, 949–963. [CrossRef]
49. Porankiewicz, B.; Axelsson, B.; Grönlund, A.A.; Marklund, B. Main and normal cutting forces by machining wood of *Pinus sylvestris*. *BioResources* **2011**, *6*, 3687–3713.
50. Kopecký, Z.; Hlásková, L.; Orlowski, K.A. An innovative approach to prediction energetic effects of wood cutting process with circular-saw blades. *Wood Res.* **2014**, *59*, 827–834.
51. Orlowski, K.A.; Ochrymiuk, T.; Hlaskova, L.; Chuchala, D.; Kopecky, Z. Revisiting the estimation of cutting power with different energetic methods while sawing soft and hard woods on the circular sawing machine: A Central European case. *Wood Sci. Technol.* **2020**, *54*, 457–477. [CrossRef]
52. Orlowski, K.A.; Ochrymiuk, T. A newly-developed model for predicting cutting power during wood sawing with circular saw blades. *Maderas Cienc. Tecnol.* **2017**, *19*, 149–162. [CrossRef]
53. Kuvik, T.; Krilek, J.; Kovác, J.; Štefánek, M.; Dvorak, J. Impact of the selected factors on the cutting force when using a chainsaw. *Wood Res.* **2017**, *62*, 807–814.
54. Yu, S.T.; Yang, C.M.; Ren, C.Q.; Luo, G. Cutting force analysis of large branch crusher based on the finite element. *Appl. Mech. Mater.* **2012**, *152*, 900–905. [CrossRef]
55. Džinčić, I.; Skakić, D. Determing the parameters of wood machinability as a function of tangential cutting force during the process of machining wood by routing. *Wood Res.* **2012**, *57*, 161–172.
56. Mandić, M.D.; Porankiewicz, B.; Danon, G.J. An attempt at modelling of cutting forces in oak peripheral milling. *BioResources* **2015**, *10*, 5489–5502. [CrossRef]
57. Krauss, A.; Piernik, M.; Pinkowski, G. Cutting Power during Milling of Thermally Modified Pine Wood. *Wood Ind./Drvna. Ind.* **2016**, *67*, 215–222. [CrossRef]
58. Durković, M.; Mladenović, G.; Tanović, L.; Danon, G. Impact of feed rate, milling depth and tool rake angle in peripheral milling of oak wood on the cutting force. *Maderas. Cienc. Tecnol.* **2018**, *20*, 25–34.
59. Colantoni, A.; Mazzocchi, F.; Laurendi, V.; Grigolato, S.; Monarca, F.; Monarca, D.; Cecchini, M. Innovative solution for reducing the run-down time of the chipper disc using a brake clamp device. *Agriculture* **2017**, *7*, 71. [CrossRef]
60. Choi, Y.S.; Cho, M.J.; Paik, S.H.; Mun, H.S.; Kim, D.H.; Han, S.K.; Oh, J.H. Factors affecting the chipping operation based on the screen size of the drum chipper. *Forests* **2019**, *10*, 1029. [CrossRef]
61. Manzone, M.; Balsari, P. Productivity and woodchip quality of different chippers during poplar plantation harvesting. *Biomass Bioenergy* **2015**, *83*, 278–283. [CrossRef]
62. Kuptz, D.; Hartmann, H. Throughput rate and energy consumption during wood chip production in relation to raw material, chipper type and machine setting. In Proceedings of the 22nd European Biomass Conference and Exhibition, Hamburg, Germany, 23–26 June 2014.
63. Ihnat, V.; Lübke, H.; Balbercak, J.; Kuňa, V. Size Reduction Downcycling of Waste Wood. Review. *Wood Res.* **2020**, *65*, 205–220. [CrossRef]
64. Dudziak, M.; Malujda, I.; Talaśka, K.; Łodygowski, T.; Sumelka, W. Analysis of the process of wood plasticization by hot rolling. *J. Theor. Appl. Mech.* **2016**, *54*, 503–516. [CrossRef]
65. Talaśka, K.; Malujda, I. Identification of thermo-mechanical properties of natural polymers with a hybrid method. *Eng. Trans.* **2016**, *64*, 635–641.
66. Ritschel, F.; Brunner, A.J.; Niemz, P. Nondestructive evaluation of damage accumulation in tensile test specimens made from solid wood and layered wood materials. *Compos. Struct.* **2013**, *95*, 44–52. [CrossRef]

67. Kokociński, W. *Wood Physical and Chemical Properties Measurements. Drewno Pomiry Właściwości Fizycznych Ichemicznych*; PRODRUK: Poznań, Poland, 2004; ISBN 83-88518-75-52004. (In Polish)
68. Bodig, J.; Jayne, B. *Mechanics of Wood and Wood Composites*; Krieger Publishing Company: Malabar, FL, USA, 1993.
69. Bachtiar, E.V. Material Characterization of Wood, Adhesive and Coating of Cultural Heritage Under Various Climatic Conditions. Ph.D. Thesis, Dresden University of Technology, Dresden, Germany, 2017.
70. Keunecke, D. Elasto-Mechanical Characterisation of Yew and Spruce Wood with Regard to Structure-Property Relationships. Ph.D. Thesis, University of Hamburg, Hamburg, Germany, 2008.
71. Aira, J.R.; Arriaga, F.; Íñiguez-González, G.; Crespo, J. Static and kinetic friction coefficients of Scots pine (*Pinus sylvestris* L.), parallel and perpendicular to grain direction. *Mater. Construcción* **2014**, *64*, e030. [CrossRef]
72. Kretschmann, D. *Mechanical Properties of Wood. Wood Handbook: Wood as an Engineering Material: Chapter 5*; General Technical Report FPL.; GTR-190; Centennial, Ed.; Department of Agriculture, Forest Service, Forest Products Laboratory: Madison, WI, USA, 2010; pp. 5.1–5.46.
73. Holmberg, S.; Persson, K.; Petersson, H. Nonlinear mechanical behaviour and analysis of wood and fibre materials. *Comput. Struct.* **1999**, *72*, 459–480. [CrossRef]
74. Garcia, J.J.; Rangel, C.; Ghavami, K. Experiments with rings to determine the anisotropic elastic constants of bamboo. *Constr. Build. Mater.* **2012**, *31*, 52–57. [CrossRef]
75. Vasic, S.; Smith, I.; Landis, E. Finite element techniques and models for wood fracture mechanics. *Wood Sci. Technol.* **2005**, *39*, 3–17. [CrossRef]
76. Torres, L.A.; Ghavami, K.; Garcia, J.J. A transversely isotropic law for the determination of the circumferential youngs modulus of bamboo with diametric compression tests. *Latin Am. Res.* **2007**, *37*, 255–260.
77. Roszyk, E.; Moliński, W.; Fabisiak, E. Radial variation of mechanical properties of pine wood (*Pinus sylvestris* L.) determined upon tensile stress. *Wood Res.* **2013**, *58*, 329–342.
78. Roszyk, E.; Moliński, W.; Kamiński, M. Tensile properties along the grains of earlywood and latewood of Scots pine (*Pinus sylvestris* L.) in dry and wet state. *BioResources* **2016**, *11*, 3027–3037. [CrossRef]
79. Krauss, A.; Moliński, W.; Kúdela, J.; Čunderlík, I. Differences in the mechanical properties of early and latewood within individual annual rings in dominant pine tree (*Pinus sylvestris* L.). *Wood Res.* **2011**, *56*, 1–12.
80. van Beerschoten, W.A.; Carradine, D.M.; Palermo, A. Compressive strength and stiffness of Radiata Pine laminated veneer lumber. *Eur. J. Wood Wood Prod.* **2013**, *71*, 795–804. [CrossRef]
81. Yapıcı, F.; Esen, R.; Erkaymaz, O.; Baş, H. Modeling of compressive strength parallel to grain of heat treated scotch pine (*Pinus sylvestris* L.) wood by using artificial neural network. *Drv. Ind. Znan. Casopis Pitanja Drv. Tehnol.* **2015**, *66*, 347–352.
82. Tasdemir, C.; Hiziroglu, S. Measurement of various properties of Southern pine and aspen as function of heat treatment. *Measurement* **2014**, *49*, 91–98. [CrossRef]
83. Sága, M.; Majko, J.; Handrik, M.; Vaško, M.; Sapietová, A. Proposal of Physical Model for Damage Simulation of Composite Structures Produced by 3D Printing. *Acta Phys. Pol. A* **2020**, *138*, 245–248. [CrossRef]
84. Sága, M.; Blatnický, M.; Vaško, M.; Dižo, J.; Kopas, P.; Gerlici, J. Experimental Determination of the Manson−Coffin Curves for an Original Unconventional Vehicle Frame. *Materials* **2020**, *13*, 4675. [CrossRef]
85. Hu, W.; Liu, N.; Guan, H. Experimental and Numerical Study on Methods of Testing Withdrawal Resistance of Mortise-and-Tenon Joint for Wood Products. *Forests* **2020**, *11*, 280. [CrossRef]
86. Kilikevičius, A.; Bačinskas, D.; Selech, J.; Matijošius, J.; Kilikevičienė, K.; Vainorius, D.; Ulbrich, D.; Romek, D. The Influence of Different Loads on the Footbridge Dynamic Parameters. *Symmetry* **2020**, *12*, 657. [CrossRef]
87. Jancar, L.; Pagac, M.; Mesicek, J.; Stefek, P. Design Procedure of a Topologically Optimized Scooter Frame Part. *Symmetry* **2020**, *12*, 755. [CrossRef]
88. Pravilonis, T.; Sokolovskij, E.; Kilikevičius, A.; Matijošius, J.; Kilikevičienė, K. The Usage of Alternative Materials to Optimize Bus Frame Structure. *Symmetry* **2020**, *12*, 1010. [CrossRef]
89. Kilikevičius, A.; Skeivalas, J.; Kilikevičienė, K.; Matijošius, J. Analysis of Dynamic Parameters of a Railway Bridge. *Appl. Sci.* **2019**, *9*, 2545. [CrossRef]
90. Krawiec, P.; Grzelka, M.; Kroczak, J.; Domek, G.; Kołodziej, A. A proposal of measurement methodology and assessment of manufacturing methods of nontypical cog belt pulleys. *Measurement* **2019**, *132*, 182–190. [CrossRef]
91. Krawiec, P.; Różański, L.; Czarnecka-Komorowska, D.; Warguła, Ł. Evaluation of the Thermal Stability and Surface Characteristics of Thermoplastic Polyurethane V-Belt. *Materials* **2020**, *13*, 1502. [CrossRef] [PubMed]
92. Zhou, Y.; Sun, Y.; Huang, T. Impact-Damage Equivalency for Twisted Composite Blades with Symmetrical Configurations. *Symmetry* **2019**, *11*, 1292. [CrossRef]
93. Hu, W.; Liu, N. Numerical and Optimal Study on Bending Moment Capacity and Stiffness of Mortise-and-Tenon Joint for Wood Products. *Forests* **2020**, *11*, 501. [CrossRef]
94. Wojtkowiak, D.; Talaśka, K.; Malujda, I.; Domek, G. Estimation of the perforation force for polymer composite conveyor belts taking into consideration the shape of the piercing punch. *Int. J. Adv. Manuf. Technol.* **2018**, *98*, 2539–2561. [CrossRef]
95. Gonzalo, O.; Jauregi, H.; Uriarte, L.G.; de Lacalle, L.L. Prediction of specific force coefficients from a FEM cutting model. *Int. J. Adv. Manuf. Technol.* **2009**, *43*, 348. [CrossRef]

96. Handrik, M.; Sága, M.; Pecháč, P.; Kopas, P. Analysis of force conditions of the hot forming machine in rolling-out of bearing ring. *Manuf. Technol.* **2015**, *15*, 821–825. [CrossRef]
97. Wojtkowiak, D.; Talaśka, K. Determination of the effective geometrical features of the piercing punch for polymer composite belts. *Int. J. Adv. Manuf. Technol.* **2019**, *104*, 315–332. [CrossRef]